Department of Physics and Astronomy
Heidelberg University

Bachelor Thesis in Physics
submitted by

Fabian Königstein

born in Mannheim (Germany)

2023

Simulation and analysis of cluster shapes in the ALPIDE monolithic active pixel sensor

This Bachelor Thesis has been carried out by Fabian Königstein at the
Physikalisches Institut, Heidelberg University
under the supervision of
Prof. Dr. Silvia Masciocchi

Abstract

One major element of the recent upgrade of the ALICE experiment at CERN is the installation of the new Inner Tracking System (ITS). Its key component is the ALPIDE chip, a CMOS Monolithic Active Pixel Sensor (MAPS) that detects ionizing particles from LHC collisions. It features high resolution and efficiency, excelling at reconstruction of primary and secondary vertices, as well as detection of low momentum particles. ALPIDE is a digital sensor, meaning that only binary information is recorded about the passing of a particle: either a pixel records the passage or not. No information about the energy of the particle is available. The scope of the thesis is to explore whether it is possible to simulate the complex effects of charge diffusion and drift in ALPIDE sensors on pixel clusters that recorded the passage of a particle, using a simple theoretical model. This can be used to try and understand if the size and shape of a cluster can be used as means towards a rudimentary identification of the particle in the digital sensor. The theoretical model is adapted and compared to data taken from beam test campaigns, in order to verify its validity.

Zusammenfassung

Ein großes Element der kürzlichen Modernisierung von ALICE am CERN ist die Installation des neuen Inner Tracking Systems (ITS). Das Herzstück desselben ist der ALPIDE Chip, ein mit CMOS-Technologie realisierter Monolithischer Aktiver Pixel Sensor (MAPS), der ionisierende Strahlung der Hauptkollision am LHC nachweisen kann. Besondere Eigenschaften sind hohe Auflösung und Effizienz, gute Leistung im Restrukturieren von primären und sekundären Vertizes, sowie der Nachweis von Teilchen mit niedrigem kinetischem Impuls. ALPIDE ist ein digitaler Sensor, stellt also Informationen über Teilchentreffer nur in binärer Form zur Verfügung; entweder ein Pixel registriert ein Treffer oder nicht. Keine weitere Information über die Energie des Teilchens ist verfügbar. In dieser Arbeit wird untersucht, ob es möglich ist die komplexen Effekte von Diffusion und Drift von Ladungsträgern auf Pixelcluster innerhalb des ALPIDE Chips mit einem einfachen theoretischen Modell zu Simulieren. Dieses Wissen kann dann benutzt werden, um zu verstehen ob die Form und Größe eines Clusters benutzt werden kann, um die Teilchenidentität mithilfe eines digitalen Sensors grob einzuschränken. Das theoretische Modell wird an Daten von vergangenen Strahltestexperimenten angepasst und mit diesen verglichen, um die Validität zu bestätigen.

Contents

1 ALICE at the LHC

The work presented in this thesis was done in the context of the ALICE experiment at the LHC, at CERN. ALICE is one of the many experiments at CERN. Scientists from 110 countries [1] investigate the building blocks of matter as well as the fundamental interactions among them. In order to do this, large detector systems, using state-of-the-art-technology, are used. The ALPIDE chip, central part of this thesis, is an example of such detectors. It was developed and is actively used by ALICE.

1.1 CERN and the LHC

CERN is an acronym which translates to *European Center for Nuclear Research*. It is an accelerator facility and research laboratory located in Geneva, at the Swiss-French border. CERN is also known for operating the Large Hadron Collider, a particle accelerator structure with a circumference of 27 km, making it currently the largest man made particle collider in the world [2]. In this ring so-called *bunches*, groups of protons or heavier atomic nuclei, are accelerated in opposite directions to ultra relativistic speeds. They are brought to head-on collisions with one another at four crossing points along the Large Hadron Collider (LHC), as shown in figure 1.

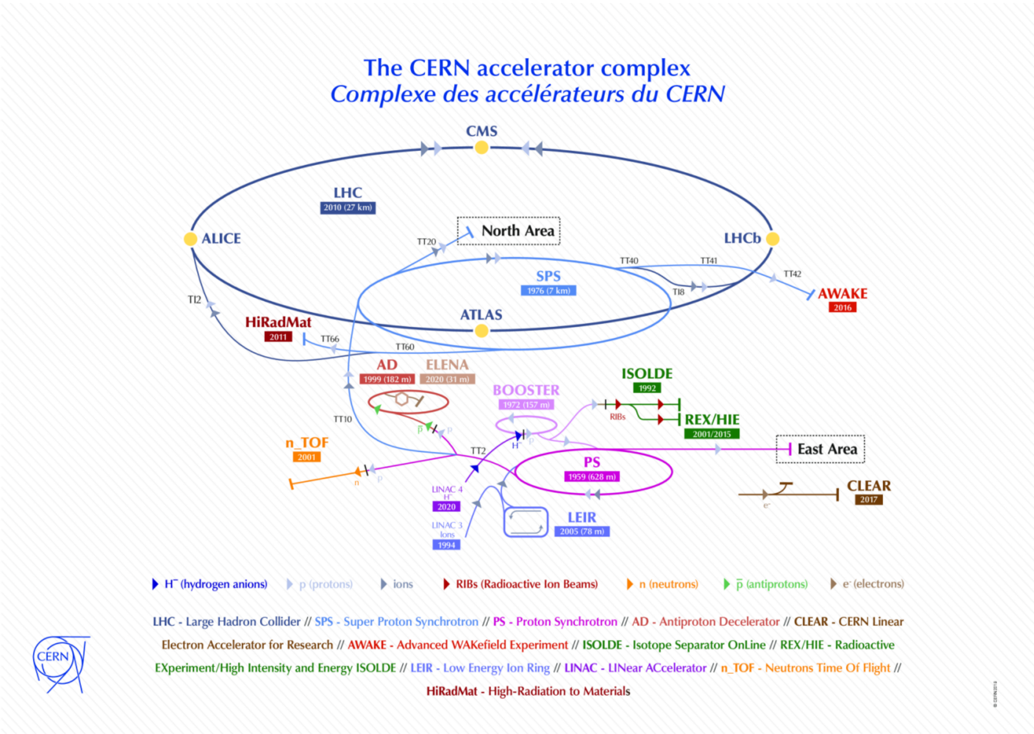

Figure 1: The CERN accelerator complex [3].

At these points, there are large experimental caverns which house the four main particle detectors of the LHC. There are A Toroidal LHC Apparatus (ATLAS) and Compact Muon Solenoid (CMS), two general-purpose detectors, which study a wide range of physics. These are the detectors that discovered the Higgs Boson. All LHC detectors study heavy quarks, subatomic particles that do not occur in normal matter and can only be created at very high energies. The Large Hadron Collider beauty (LHCb) physics program focuses on flavor physics, with special emphasis on the bottom (or beauty) quark. See [4] for further reading. Is the second-heaviest quark in the standard model [2].

The location of the fourth detector can be seen to the left of figure 1. It is called A Large Ion Collider Experiment (ALICE), and studies the formation and properties of the quark-gluon-plasma. It is an exotic state of matter, which gets formed at high energies (temperatures) and densities. These are accessible in particle collisions provided by the LHC.

1.2 A Large Ion Collider Experiment

ALICE is a detector of $16\,\mathrm{m} \times 16\,\mathrm{m} \times 26\,\mathrm{m}$ in size, and is placed around the LHC at the so-called Point 2. The whole detector is located over 50 m below the surface. The luminosity of the LHC[1] in Run 3 is $6.4 \times 10^{27}\,\mathrm{cm}^2\,\mathrm{s}^{-1}$ for Lead-Lead collisions [6]. This is higher than the ALICE readout can support in Run 3, at 50 000 lead-lead collisions per second [7]. This rate in turn has been improved 50-fold over Run 2.

The purpose of ALICE is to study the properties of the quark-gluon-plasma (QGP), which is being produced in heavy-ion collisions and has a lifetime in the order of $10\,\mathrm{fm/c}$, or $1 \times 10^{-23}\,\mathrm{s}$ [8]. The QGP is a very hot state of matter, where the elementary particles that form hadrons have their confinement lifted under high energy densities in a manner similar to a plasma. They become quasi-free and form a fluid-like medium for a short time. The QGP behaves like an almost perfect fluid, with very low viscosity, the exact value being still in question.
To measure the viscosity and other parameters, the production of hadronic and leptonic particles stemming out of the QGP is examined. To extract this information, ALICE comes with a multitude of subdetectors, each designed with their own purpose in recording specific particle properties contributing to the goal of ALICE. [9]
The subdetectors can be grouped according to their respective tasks in ALICE. They track particles, determine charge, measure momentum or characterize the collision geometry that just happened inside the detector. Figure 2 shows a model of ALICE with some marked main detectors. The different purposes of the labeled parts are quickly explained here, but the focus is set on the Inner Tracking System 2 (ITS2), where the Alice Pixel Detector (ALPIDE) sensors that are utilized in this thesis are used.

The large surrounding L3 magnet produces a magnetic field of 0.5 T in the ALICE detector [11]. This field forces charged particles on curved flight paths.

[1] Measure for interactions/time in colliders, see [5]

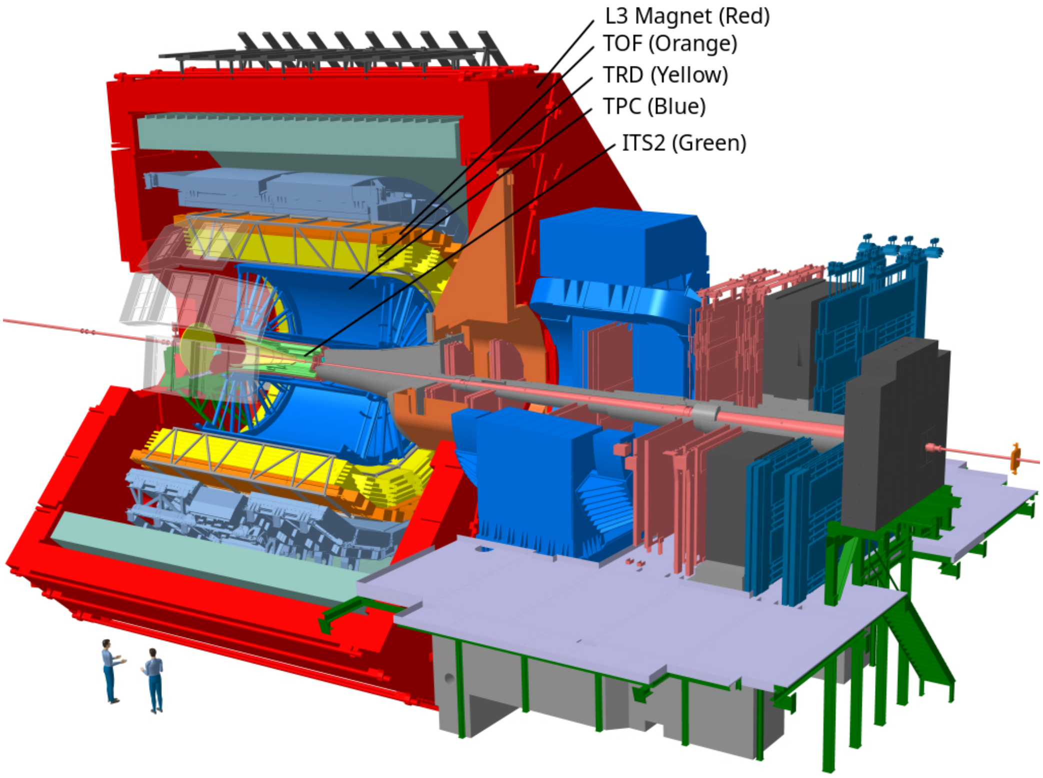

Figure 2: The ALICE detector as a 3D cutaway model [10], some subdetectors have been marked.

The Inner Tracking System and the Time Projection Chamber (TPC) accomplish tracking by determining points in space, where charged particles passed through these detectors. Using these points, the particle trajectory is reconstructed. This process is called tracking. The bending radius of the resulting track in a magnetic field provides a measurement for the particle momentum. Additional information such as the specific energy loss in the detector material or the time of flight is used to identify the particles [12].
The ITS2 is positioned closest to the collision point in the center of ALICE, to precisely track passing charged particles. The ITS2, the successor of the ITS, as it has recently been upgraded in the LHC Long Shutdown 2 (LS2) is a pixel detector. It uses silicon sensors which detect charge deposited in their pixels by ionizing particles. These sensors are called ALPIDE and the ITS2 is made of a total of about 24000 of them, covering a total area of $10\,\mathrm{m}^2$. The ITS2 can reconstruct their trajectory in the center of the detector with a precision of around $5\,\mu\mathrm{m}$ [13]. This is needed to identify so-called *secondary vertices*, which are the decay points of very short-lived particles. These are created at the primary vertex, travel for a short time and then decay into more stable particles before reaching any detectors. For this reason, they can only be measured via the reconstruction of their decay products and decay vertex. This shows the need for high resolution position tracking, to resolve tracks that do not originate from the primary collision.

The TPC is enveloping the ITS2. It is a barrel shaped detector with the end caps oriented normal to the beam direction. Marked as the blue detector in figure 2, the TPC is a gas chamber, where charged particles ionize gas atoms such that electron ion pairs are left behind on their path. These liberated charges subsequently drift by virtue of an electric field towards the end caps of the cylindrical chamber. There, the timestamp, position and amount of charge arriving at the individual detector pads are registered.

Outside the TPC, the Time Of Flight (TOF) detector is located. It measures the time it took each particle to arrive from the primary vertex to this detector. This time is determined with very high accuracy of less than 1×10^{-10} s, or 100 ps [12]. Such accurate time of flight measurements allow for precise velocity calculation. These pieces of information aid further in resolving ambiguities from other detectors in terms of particle identification.

1.3 The ITS2

As explained in the previous section, the purpose of the Inner Tracking System is to do precision particle tracking. It has been upgraded during the LHC LS2 of 2019-2022 to the ITS2.
Also, ITS2 was reworked to conduct more precise tracking and vertex reconstruction than its predecessor, while reducing the material budget significantly and giving up particle identification performance [14].

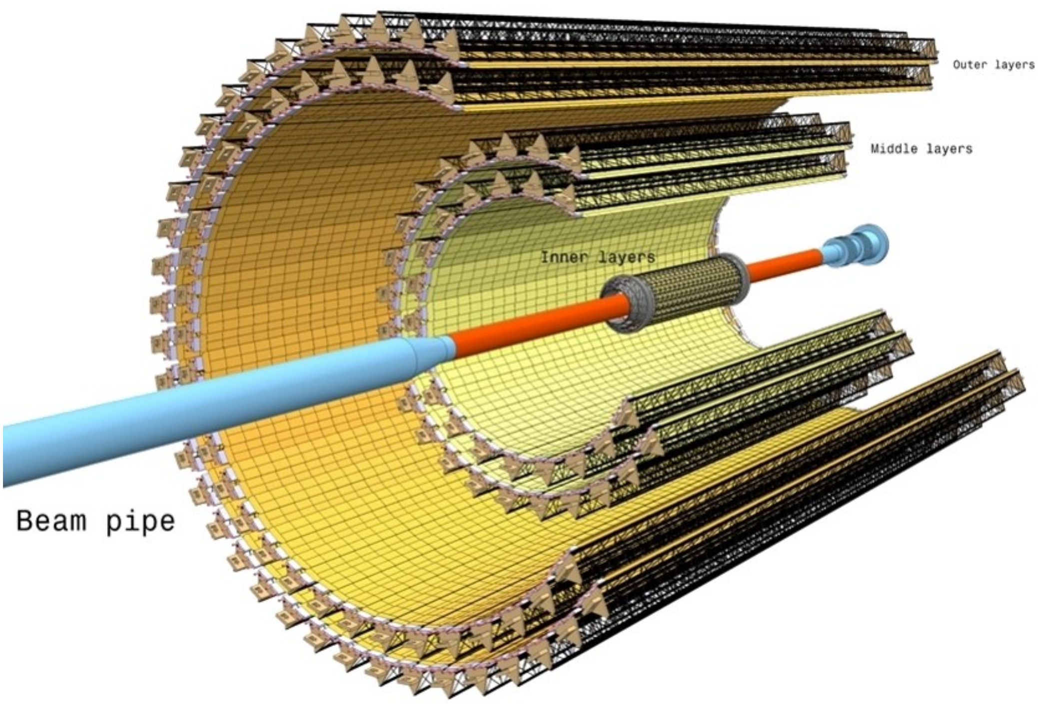

Figure 3: The ITS2 layout, with all seven detector layers [7].

Figure 3 shows the ITS2 layout, as currently installed in ALICE. One can easily see the new smaller beam pipe (red) which was installed during the LS2. This allows the inner layers to be placed closer to the interaction point.

Its wall thickness was reduced, and the whole new beam pipe is made out of beryllium to reduce material budget [13].
The detector itself and other support structures can scatter incoming particles, distorting their trajectories. A measure for electron interaction with matter is the radiation length. It is material specific, and describes the mean distance over which an electron loses all but $1/e$ of its original energy traversing this material [15]. A certain percentage of radiation length (x/X_0 [%]) is called the *material budget*. Reducing scattering inside a detector is now synonymous to reducing its total material budget.
The ITS2 is designed with a low material budget in mind. Especially particles in the low-momentum region are more easily scattered at a large angle [15]. To better achieve low scattering, the support structures are designed as lightweight as possible. The ITS2 is composed of seven cylindrical layers, ranging from an inner radius of 2.3 cm up to an outer barrel radius of 39.3 cm [7]. The length of the ITS2 modules also varies greatly, the inner barrel is 27 cm long, the outer layers up to 148 cm. In total the ITS2 has a combined 12.6×10^9 pixels [7].
There is over $10\,\mathrm{m}^2$ of active detector surface built into the ITS2. This is so far the largest pixel detector [7] of MAPS based on the CMOS process, which has been realized. Thanks to the requirements of ALPIDE chips [16] a thermal output density of less than $40\,\mathrm{mW\,cm^{-2}}$ is achieved [16]. This is especially useful for limiting cooling needs to reduce the material budget.

ITS2 utilizes monolithic active pixel sensors (MAPS). This means, unlike hybrid pixel sensors, that the sensor and readout electronics are integrated together in one piece of silicon. Hybrid pixel sensors use solder bump-bonds to join a sensor and a readout chip together. This makes MAPS significantly thinner and lighter, as ALPIDE chips are 50 µm thick in the inner barrel and 100 µm in the outer barrel, compared to hybrid pixel sensor counterparts of multiple hundred µm in thickness [7]. One chip is $3\,\mathrm{cm} \times 1.5\,\mathrm{cm}$ large [17] and can detect particles passing through the pixels on a matrix with a position resolution of less than 5 µm. [16]
To further improve the measurement of short-lived particles, another ITS upgrade is planned and will be installed in the LS3 starting in 2026 [18]. Three layers of bent MAPS will then replace the current three inner layers of ITS2. The ITS3 will be closer to the beam pipe than ITS2, with an inner barrel radius of 18 mm [19]. Additionally, the detector area itself will be composed of large sensors 20 µm to 30 µm thick, which will be bent to increase structural rigidity. Together with reduced power needs, the new ITS design allows for significant reduction of support structure. This also means a significant reduction of material budget from $0.3\,\%\,x/X_0$ to $0.05\,\%\,x/X_0$ per layer.

2 Interaction of charged particles with matter

This section will be about the interactions of charged particles with matter. Charged particles carry a non-zero electric charge. All free particles carry a multiple of the elementary charge, e. $1\,e$ is the charge of the proton. Single quarks have a fractional charge of multiples of $\frac{1}{3}$ e as their particle charge. But they do not exist as unbound individual particles traveling freely. The lightest charged particle is the electron, having the opposite charge of the proton.

2.1 Standard Model

The Standard Model (SM) of particle physics is the basis for the description of the subatomic world in modern physics. Figure 4 is a representation of

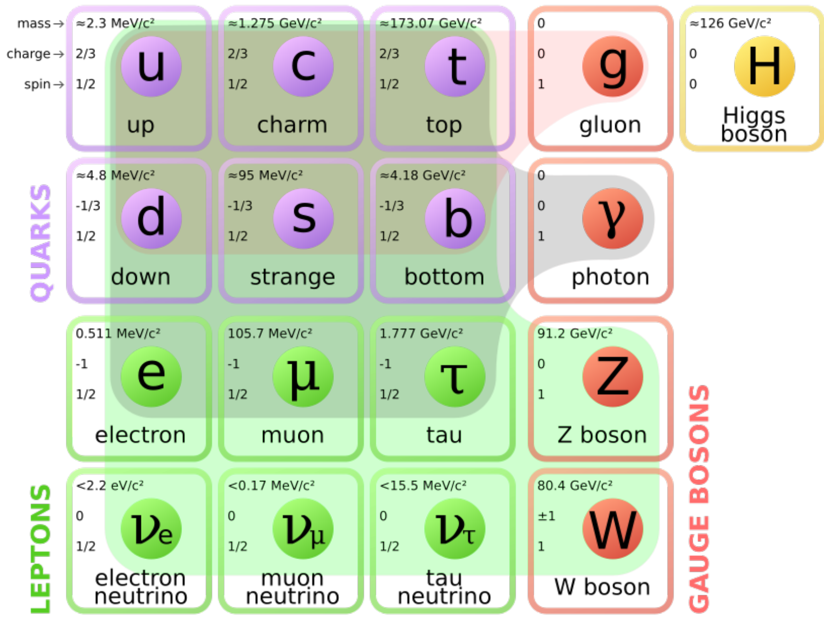

Figure 4: Standard model of particle physics[20]

the elementary particles in the Standard Model, the quarks and the leptons. This figure also shows indicated force groupings with slight colored hues. The red gauge bosons on the right-hand side are the particles that couple to the quarks or leptons, mediating the three types of forces that are described by the Standard Model. These forces can be ranked by the range of their typical interaction length and the relative force strength, as can be seen in table 1. The strongest and shortest-ranged is the strong force, mediated by the gluon at ranges of the order of 1 fm. At larger distances of up to ≈ 5 fm, mesons take over that mediator role. The gluon couples to the color charge. Quarks can have one of three color charges: red, green or blue. Gluons can only mediate between quarks of different color charge. Gluons make quarks form states of quark-antiquark (*mesons*) or three quarks (*baryons*). In the case of baryons, the included quarks have all three colors. Mesons on the other

Force	Strong	Electromagnetic	Weak
Boson	Gluon g	Photon γ	$W^{\pm}$, Z
Mass [GeV/c^2]	0	0	80.4 and 91.2
Relative strength	1	1×10^{-3}	1×10^{-8}
Reach [fm]	≈ 1	∞	< 1
Charge	color charge	electric charge	hypercharge

Table 1: Comparison of the forces described by the Standard Model [21], p.6

hand are made from color-anticolor pair, and thus are also color neutral to the outside. A proton consists of two up and one down quark, alternatively written as *uud*. The neutron is made of *udd*, two down and one up quark. All baryons are made from three quarks, and can only have an integer charge. Mesons only consist of a quark and anti-quark, which form a pair. They also can only form to states that have an integer charge number.

The weak interaction is the weakest of the three. It is responsible for the decay of atomic nuclei with the β decay branch. Unstable particles, for example particles with strangeness, also decay via the weak interaction. It is mediated by either the W^+, W^- or Z boson, which, unlike the other gauge bosons, have a rest mass.

The electromagnetic force is the longest range of the forces in this model. It is mediated by the photon. It for example provides the necessary attraction between negatively and positively charged particles such as protons and electrons. This way they can form atoms, complete with their electron orbitals. It couples to all particles which carry electrical charge.

2.2 Ionizing radiation

Particles which carry enough kinetic energy to liberate electrons from atomic bound states are called *ionizing*. Ionizing radiation refers to all radiation which has this potential. It is dangerous for biological matter, because ionization has the potential to destroy chemical bindings. This can cause biological malfunctions or destruction of important molecules in living cells.
When passing through materials, an ionizing particle loses energy because of different interactions with matter. The amount of lost energy per traveled distance is greatly dependent on the type of radiation and the type of material traversed.

2.2.1 Sources

Sources of ionizing radiation are widespread and large in energy ranges or particle type. There is cosmic radiation, which consists at the earths surface almost entirely of muons. There are also radioactive nucleids found naturally in the Earth's crust, or artificially created in nuclear reactors. Depending on the element and nuclide they emit alpha, beta or gamma radiation.

Alpha Alpha particles are helium nuclei. They only have a very short range in air, and typically cannot reach further than a few centimeters. Since they contain two protons, they carry 2 e positive charge. Alpha particles are usually parted from a main decaying nucleus in a nuclear reaction, leaving behind the now lighter core.

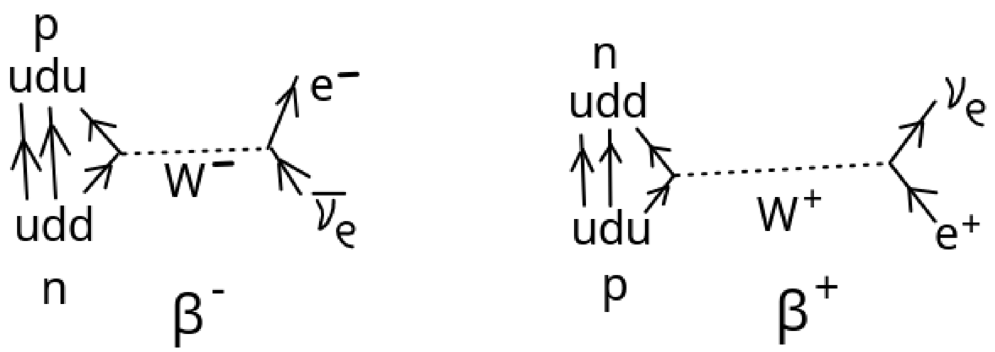

Figure 5: β^- and β^+ decay Feynman diagrams respectively.

Beta Beta radiation are either electrons (β^-), or positrons (β^+). The respective Feynman diagram can be seen in figure 5. An electron is emitted when a neutron inside the core is converted into a proton and an anti-electron neutrino. Generally this happens for free neutrons or in neutron-rich atom nuclei. The opposite direction is energetically forbidden for protons, since the rest mass of the neutron is higher than the proton. However, it happens for some proton-rich nuclei where the atom gains more than $2\,\mathrm{m_e c^2}$ of binding energy. This energy difference is the minimum to counteract the higher neutron mass, and includes the loss of one electron from the shell. The $\beta^\pm$ decay is a three-particle decay, where the proton has 99.95% of the mass [22]. Therefore, it receives up to around 700 eV of kinetic energy [23]. The rest is shared between the neutrino and electron, leading to an energy spectrum of beta radiation.

Gamma Gamma radiation is not a direct result of a nuclear process in the sense that it does not change the makeup of a nucleus. For example excited nuclei that just underwent a nuclear reaction can de-excite themselves by emitting a photon. This photon usually has a higher energy than visible or X- radiation and therefore is called gamma radiation.
In terms of radiation protection, alpha particles can be stopped by an aluminum foil or a sheet of paper.
Beta decay electrons can usually also be protected against, but for this case high density materials such as lead are not advisable. This is because the electrons stopping in the absorber will emit more gamma bremsstrahlung. For radiatively emitted electrons though a few millimeters of aluminium is usually enough.
Gamma rays are the most penetrating kind of ionizing radiation. Some-

times even centimeters of lead are not enough to stop the ionizing effects completely.

2.3 Energy loss

As hinted at previously, the amount of energy lost is greatly dependent on a multitude of factors. Also there are multiple mechanisms which lead to particles losing energy in matter. Their contribution to the total energy lost shifts depending on the particle energy.

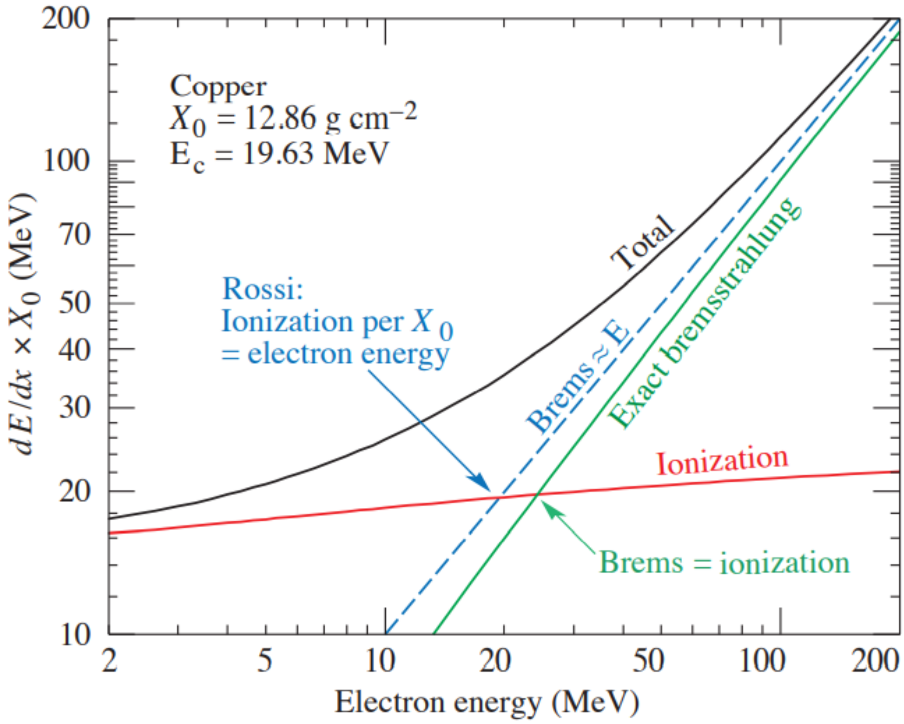

Figure 6: Electron energy loss comparison [15].

How ionization and bremsstrahlung contribute can be seen in figure 6. In the energy range of up to a few GeV that is important for the ALICE experiment and therefore the ALPIDE chip, the main mechanism is energy loss via ionization, with one exception.

For electrons over 20 MeV the leading contribution to energy loss is the bremsstrahlung process [15]. However, this interaction produces hard photons, which do not ionize matter by themselves.

For bremsstrahlung to occur, a third particle is needed. This is because any physical process conserves energy and momentum. Since photons have zero rest mass (see figure 4), a charged particle cannot just emit a photon. Another particle is needed to carry the momentum away and make the process possible. It does this via a coulomb interaction, using a second photon via a nearby nucleus. Figure 7 depicts this interaction as a Feynman diagram.

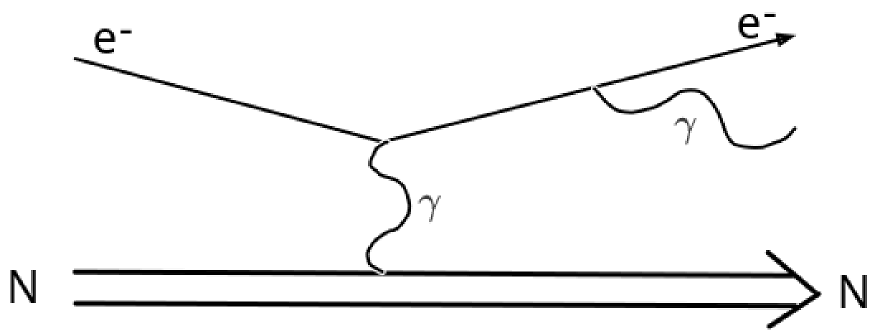

Figure 7: The bremsstrahlung process as a Feynman diagram.

2.3.1 Ionization

Ionization is the main process via which charged particles traversing the ALPIDE detector liberate charge in it. Since the majority of space in matter is occupied by the electron orbital hulls of atoms, any interaction with them is far more likely than any interaction with nuclei. Electron binding energies can be as low as a few tens of eV [24]. If there is enough energy transferred from passing charged particles, they will liberate electrons from the atoms and leave behind ions. These free electrons can now diffuse through matter, or drift along electric fields. The amount of electrons liberated is directly dependent on the energy lost by the ionizing particle. Since electrons that receive a large amount of energy can themselves knock out electrons from atoms, one can assume that eventually every electron has below one binding energy in excess kinetic energy. This would mean that the number of electrons liberated is proportional to the energy deposited in the sensitive area. The average amount of energy lost by a heavy charged particle via ionization is described by the Bethe-Bloch formula [15][25]

$$\left\langle -\frac{dE}{dx} \right\rangle = Kz^2 \frac{Z}{A}\frac{1}{\beta^2}\left[\frac{1}{2} ln\left(\frac{2m_e c^2\beta^2\gamma^2 W_{max}}{I^2} - \beta^2 - \frac{\delta\left(\beta\gamma\right)}{2}\right)\right]. \quad (1)$$

z: Charge of incident particle [e]
K: Constant; $K = 4\pi N_A r_e^2 m_e c^2 = 8.988 \times 10^{16}\,\mathrm{J\,m^2\,mol^{-1}}$
$\mathrm{N_A}$: Avogadro constant, particles in one mol (6.022×10^{24})
$\mathrm{r_e}$: Classical electron radius; $2.818 \times 10^{-15}\,\mathrm{m}$
$\mathrm{m_e}$: Electron mass; $9.109 \times 10^{-31}\,\mathrm{kg}$
c: Light speed in vacuum: $2.998 \times 10^{8}\,\mathrm{m\,s^{-1}}$
$\mathrm{W_{max}}$: Maximum energy transfer in a single interaction,
$W_{max} = \frac{2m_e c^2\beta^2\gamma^2}{1+2\gamma m_e/M+(m_e/M)^2}\left[\mathrm{kg\,m\,s^{-1}}\right]$
β: Velocity fractional to light speed; $\frac{v}{c}$
γ: Lorentz gamma factor; $\gamma = \frac{1}{\sqrt{1-\beta^2}}$
Z: Atom core charge number of absorber [e]
A: Molar mass of absorber $\left[\mathrm{g\,mol^{-1}}\right]$
e: Absolute charge carried by the electron; $1.602 \times 10^{-19}\,\mathrm{C}$
I: Average ionization energy of traversed medium [eV]

$\delta(\beta\gamma)$: Density effect correction; $\delta(\beta\gamma) = ln\left(\frac{\hbar\omega_p}{I}\right) + ln\,(\beta\gamma) - \frac{1}{2}$
$\hbar\omega_\mathrm{p}$: Plasma energy of the target medium; $\hbar\omega_p = \sqrt{4\pi N_e r_e^3} m_e c^2/\alpha$ [eV]
$\mathrm{N_e}$: Target medium electron density in units of r_e
α: Fine structure constant; $\frac{1}{\alpha} \approx 137.036$

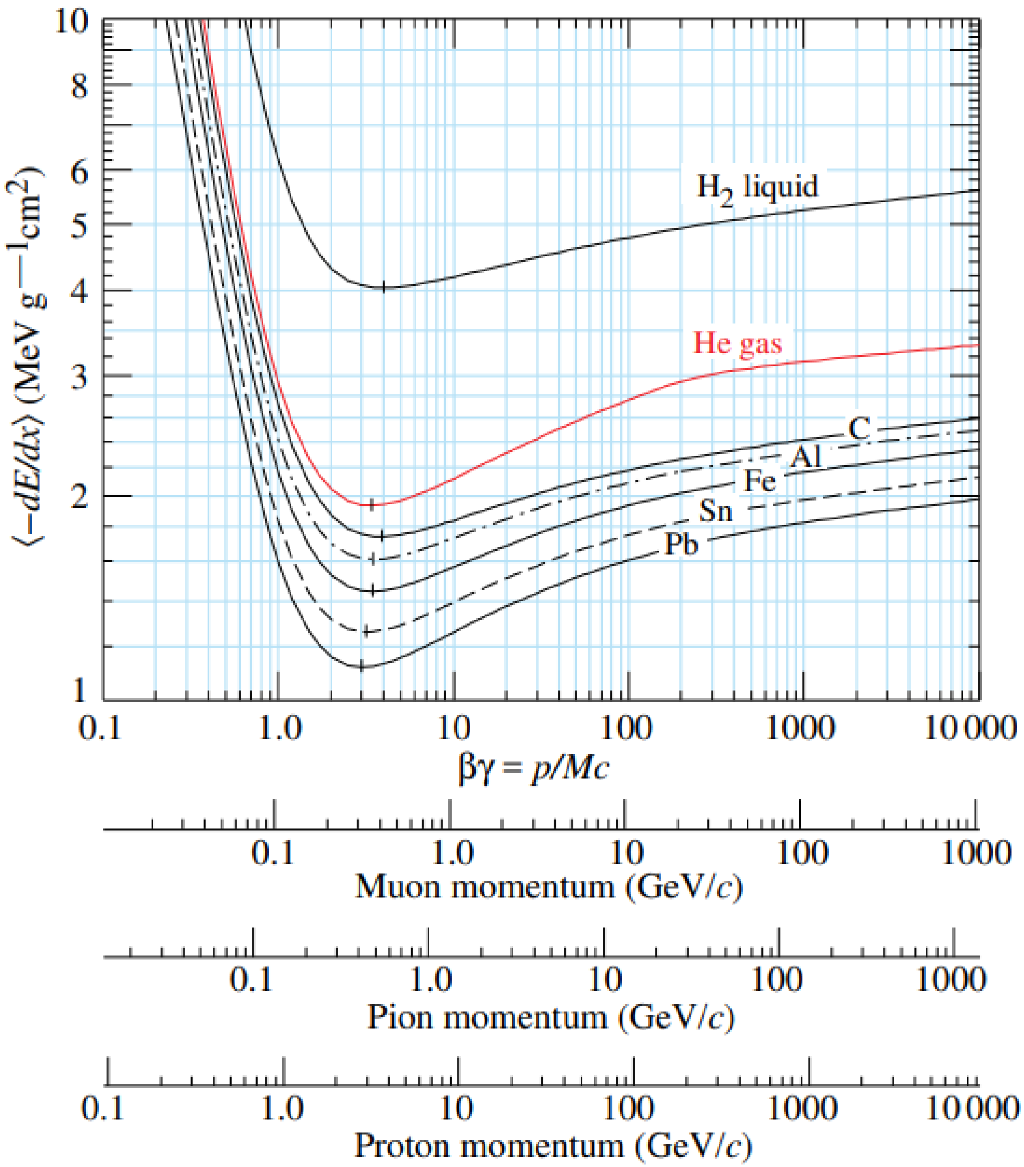

Figure 8: Bethe Bloch formula drawn with multiple representations of target media and particle species[15].

The equation can be further divided by the density of the absorber $\left(\rho\ \left[\frac{\mathrm{g}}{\mathrm{cm}^3}\right]\right)$. This changes the unit from $\mathrm{MeV\,cm^{-1}}$ to $\mathrm{MeV\,cm^2\,g^{-1}}$. This additional step is called density normalization.
Using this method, Bethe-Bloch curves for different absorbers and particles sit on top of each other, as seen in figure 8. They all exhibit a minimum at $\beta\gamma \approx 3$ to 4.
Both axes have a logarithmic scale. On the x-axis the beta gamma factor is

shown which can be calculated using:

$$\beta\gamma = p/E = p/(Mc)\,. \tag{2}$$

The total energy of a particle is denoted with E, p is its momentum and M refers to its rest mass. For different particle species, accounting for different rest masses, different x-axes are drawn. Each of them has an offset [2], to account for a higher or lower rest mass. The y-axis is the average energy lost via ionization in MeV per traveled cm and per absorber density.
Finally, there are multiple energy loss functions drawn for different kinds or absorber materials. Because of the Z/A dependence, lead has the lowest average energy loss per length per density. Lower mass elements generally have a higher absorption per density, with liquid hydrogen having the highest value at any point of the function. The general Bethe-Bloch shape is not dependent on particle type, nor absorption material.
The Bethe-Bloch function is valid for $0.1 < \beta\gamma < 1000$. The formula however does not take bremsstrahlung into account, which is a process important for electrons over 20 MeV of kinetic energy, a $\beta\gamma$ of ≈ 40 [15]. Electrons in general are somewhat special and need extra consideration.

At $\beta\gamma \approx 1000$ radiative effects begin to be important.
For qualitative purposes, $\langle -dE/dx \rangle$ is a function of $\beta\gamma$. At high energies, a mass (M) dependency is introduced with W_{max}. The function first falls steeply because of its direct antiproportionality to β^2 and approaches the minimum ionizing region at $\beta\gamma = 3$ to 4. It then rises inevitably as the argument of the logarithmic term increases [15]. One part is contributed by the explicit dependence $\beta^2\gamma^2$ of the logarithmic term. This is corresponding to the relativistic boost of the electric field. But this effect is cancelled, as at some point the field polarizes the medium and cancelling the rise of the logarithmic term. This effect is in turn represented by the density-effect correction $\delta(\beta\gamma)$. A smaller part is the implicit $\beta^2\gamma$ dependence of W_{max}, the maximum possible energy transfer in one collision. Hard collision events continue to elevate the average energy loss for higher energies.

The energy loss process is statistical in nature and exhibits fluctuations from the many ionization and excitation processes. The most probable energy loss differs from the average energy loss, and is described by a Landau distribution. The most probable energy loss is lower than the average, especially for high energies. The most probable value does not continue to rise, it approaches a "Fermi plateau". Only the maximum possible energy transfer extends to higher energies, thus influencing the average.

2.4 Detection

Detectors can employ different kinds of mechanisms to detect particles. One possibility is via the process of ionization. In noble gases, as usually used

[2] The scale is logarithmic, and the offset value is a multiplication. This results in the axes shifted by a constant value.

in gas detectors, atoms get ionized by radiation. In this process, the energy needed for ionization is in the order of tens of eV to be ionized [24]. The electrons and ions can then drift with an electric field, and read out by electrodes. Also, electrons can be amplified using electron multiplication, often times realized via acceleration of electrons in high electric fields. In the ALICE TPC, electrons drift towards the end caps along an axial electric field. In the Run 3 TPC version electrons are read out using Gas Electron Multiplier (GEM) foils. These create a strong electric field in their vicinity, allowing for charge amplification [26].

With solid state technology, a process utilizing ionization in solid matter can be realized. Using advancements in solid state physics knowledge, silicon chips advanced to a level where such an implementation is feasible. In ALPIDE, charge is collected from the epitaxial layer of only a few tens of µm thickness. Here electrons are freed from their positions in the silicon lattice. See section 3.2 for details. The electrons diffuse through the silicon, and either recombine or reach a collection diode of the chip. In the presence of the electric field from the diode they start drifting, and are collected. This signal is then electronically amplified, digitalized and read out.

3 Semiconductors and ALPIDE

Inside solid semiconductors, electron-hole pairs are created instead of electron-ion pairs as is the case for gases. Electron-hole pairs have the advantage that only a few eV are needed for their generation. This significantly lower energy leads to proportionally more free charge carriers than in gas. The significantly higher ionization yield enables a reduction of material thickness, since for less material the same amount of deposited charge as in gas can be gained. This allows for a significant compacting of detectors.

To understand the basics of ALPIDE operation, an introduction to semiconductor physics is given.

3.1 Semiconductors

3.1.1 Intrinsic Semiconductors

Electrical continuity in metals is achieved because some electrons are delocalized. These electrons are not bound to a single atom, but they are free to travel through the metal lattice. This is why as soon as there is a potential difference, current flows to nullify this difference.

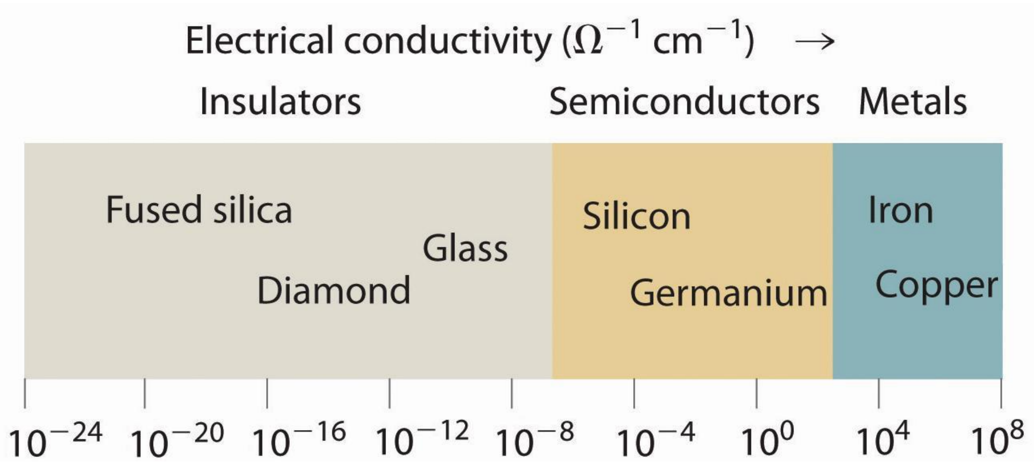

Figure 9: Electric conductivity for different element types [27]. (modified)

In insulators, electrons remain bound to their atoms, and cannot move between them. This localization leads to electrically insulating properties. Semiconductors are in between these two worlds, having an intermediate electrical conductivity. This can be seen in figure 9, where different materials are ordered against their electrical conductivity.
Atoms in a crystal can be ionized just like gas atoms. Ionization in this context refers to electrons of atom hulls are free to travel in the medium. In solid bodies this is synonymous to an electron transitioning from the energy level of the valence band to the higher energy conduction band. The bound electron energy states are part of the valence band, while free electrons are part of the conduction band. The minimal energy to excite electrons from

the valence to the conduction band inside solid bodies is called band gap. A simplified model of band gaps for different material types is shown in figure 10.

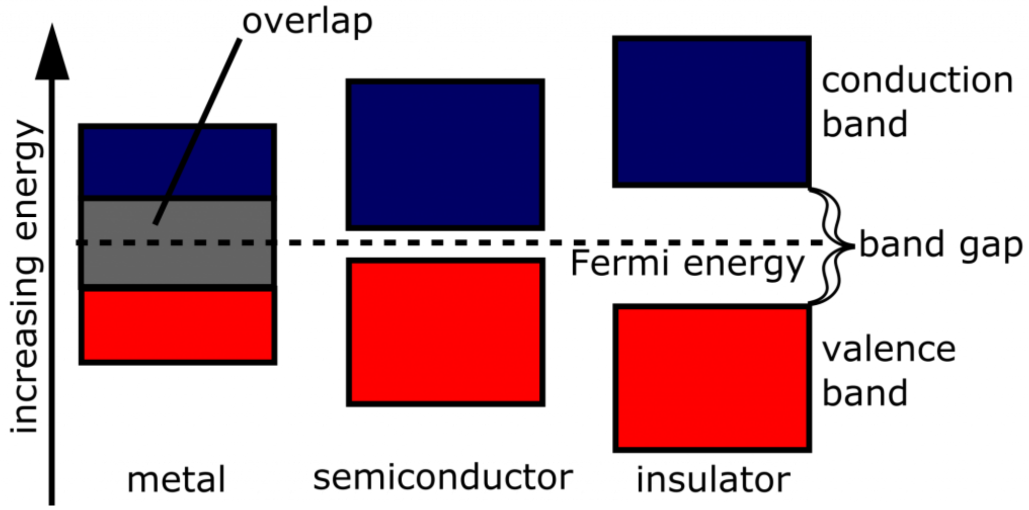

Figure 10: Band separation for different element types [28] (modified).

Semiconductors are all materials where this band gap is smaller than for insulators, but not overlapping as they are for metals. Metallic conductivity occurs both when the valence and conduction bands overlap, or when there is one band neither fully occupied, nor fully vacated.

In between the valence and conduction band energy region is the Fermi energy level. The Fermi energy is the maximum energy value an electron can have, at 0 K temperature. Since no two fermions can occupy the same quantum state, electrons get forced to occupy higher energy states. If the temperature is higher than 0 K, electrons can be additionally excited by thermal energy. Since thermal excitation energies at room temperature are only around 0.025 eV, few electrons get excited to conduction bands by thermal energy alone [29]. An increase in temperature also increases a semiconductor's conductivity, in contrast to metals. The energy distribution of electrons relative to the Fermi-energy is described by the Fermi-Dirac distribution [30]

$$f(E) = \frac{1}{1 + \exp\left(\frac{E - E_F}{k_B T}\right)}. \tag{3}$$

E_F: Fermi energy of the solid [J]
k_B: Boltzmann constant, $1.380\,65 \times 10^{-23}\,\mathrm{J\,K^{-1}}$
T: Temperature [K]

Under normal conditions, the valence bands are almost fully occupied, while the conduction bands are mostly empty. If one electron gets excited to the conduction band, it leaves behind a hole, which can be seen as a positive charge carrier. If this pair manages to separate enough from another, they can travel the lattice and contribute to conduction. In the case of an external electric field they will travel in opposite directions, because of their opposite charge. For all intrinsic semiconductors the number or free positive and negative charge carriers is equal. The intrinsic carrier concentration n_i is proportional to [30]

$$n_i \propto T^{\frac{3}{2}} exp\left(-\frac{E_g}{2k_B T}\right). \tag{4}$$

$\mathrm{E_g}$: Band gap energy at 0 K [J]

In silicon the band gap is 1.12 eV wide. Under normal conditions at $T \approx$ 300 K the intrinsic carrier concentration is $n_i = 9.65 \times 10^9\,\mathrm{cm}^{-3}$[31] [3]. It is largely controlled by the ratio of thermal energy to the band gap. Minority charge carrier concentration together with the mobility

$$\mu_i = \frac{v_i}{E} \tag{5}$$

μ_i: Mobility $\left[\frac{\mathrm{m}^2}{\mathrm{Vs}}\right]$
$\mathrm{v_i}$: Electron or hole drift velocity $\left[\mathrm{m\,s^{-1}}\right]$
E: Electric field applied across the semiconductor $\left[\mathrm{V\,m^{-1}}\right]$

dictates the resistivity of the semiconductor material. Mobilities for electrons and holes are never the same. Example values are: $\mu_n \simeq 1360\,\mathrm{cm^2\,V^{-1}\,s^{-1}}$ and $\mu_p \simeq 460\,\mathrm{cm^2\,V^{-1}\,s^{-1}}$ at 300 K in $n_i = 10^{14}\,\mathrm{cm}^{-3}$ doped silicon. In the usual semiconductors, the mobility for electrons is consistently greater than for holes. This remains true for any given doping concentration and temperature [29]. The conductivity can be calculated as

$$\rho = \frac{1}{\sigma} = \frac{1}{e(n_n\mu_n + n_p\mu_p)}. \tag{6}$$

ρ: Resistivity $[\Omega\,\mathrm{m}]$
σ: Conductivity $\left[\frac{1}{\Omega\mathrm{m}}\right]$

Under normal conditions the intrinsic resistivity of silicon is $3.2 \times 10^5\,\Omega\,\mathrm{cm}$ [32]. However, it depends a lot on slight impurities and crystal structure defects.
The maximum drift velocity is around $10^5\,\mathrm{\mu m\,\mu s^{-1}}$ for electrons in ultrapure silicon [29].
The diffusion coefficient can be calculated using the Einstein relation [29]

$$D_i = \frac{k_B T}{q}\mu_i. \tag{7}$$

$\mathrm{D_i}$: Diffusion coefficient $\left[\mathrm{cm^2\,s^{-1}}\right]$

This coefficient is $36\,\mathrm{cm^2\,s^{-1}}$ and $12\,\mathrm{cm^2\,s^{-1}}$ for electrons and holes respectively [33]. This is by orders of magnitude slower than drift.

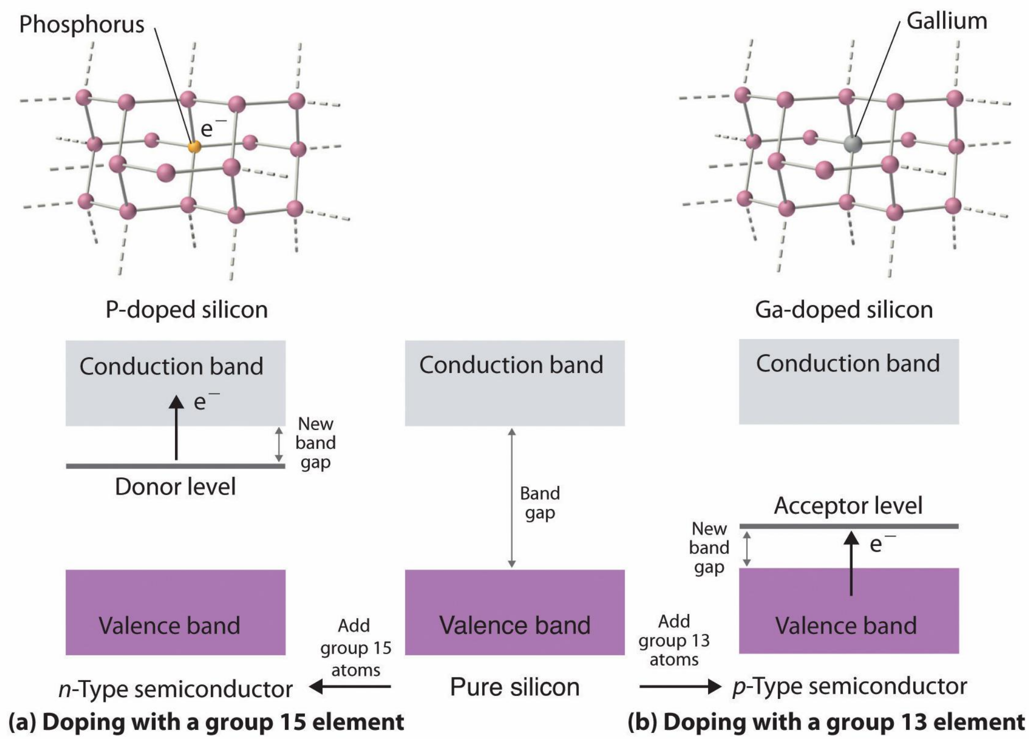

Figure 11: Doping overview for silicon as the base semiconductor[27] (modified).

3.1.2 Extrinsic semiconductors

Doped semiconductors are called extrinsic, because their properties are inherited from impurities deliberately introduced into the silicon crystal.
Specifically conductivity can be modified with the introduction of such very low concentration foreign materials in the otherwise mostly pure and crystalline structure. Examples of dopants would be phosphorus, antimony, boron or gallium. How the doping modifies the band structure can be observed in figure 11. These impurities are usually introduced in the range of $\approx 10^{-2}$ to $10^{-6}\%$ [34]. The introduced atoms replace one silicon atom in the lattice. They are either pentavalent or trivalent. This means they either have 3 or 5 electrons in their valence orbitals, the ones which form chemical bindings. Since silicon is tetravalent, the impurity either will form bonds with the silicon lattice and either leave a hole, if a bond is not complete, or introduce an extra electron. These are called majority charge carriers, since they are in excess of the respective minority charge carriers.

3.1.3 The PN-Junction

An important part of electronics is the p-n junction. It is created when positively doped and negatively doped silicon is brought into contact. This junction behaves vastly different from either material alone. It conducts

[3] See more in [30] under section 2.1

current passing through in one direction, but does not allow the reverse direction. This is called a diode.

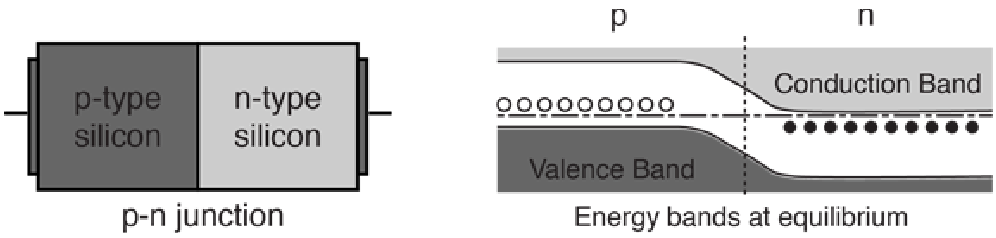

Figure 12: Simple pictogram of a p-n junction [35].

To the right side of figure 12 the internal junction energy bands are drawn. The empty circles represent the holes from a p-type, and the full dots represent the electrons from an n-type semiconductor. The center line represents the Fermi energy level, staying constant within the structure. Since the two involved semiconductor types differ in their doping qualities, the valence and conduction bands do not share the same energy.

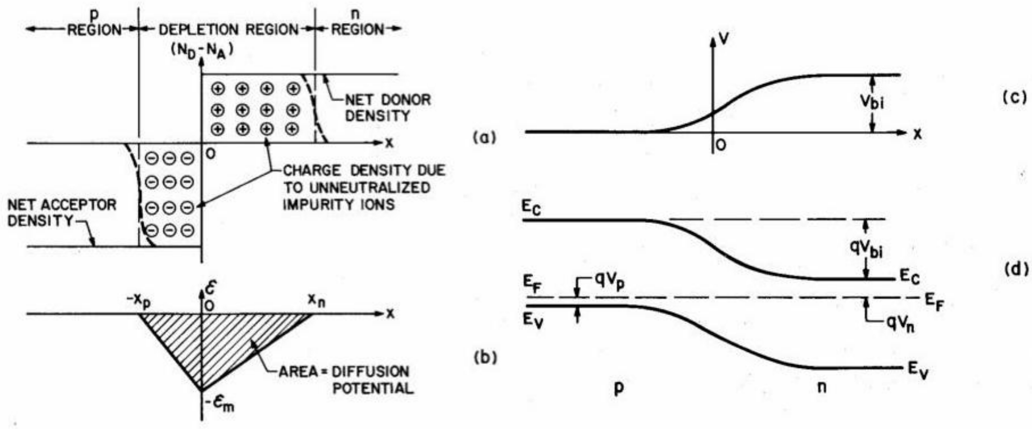

Figure 13: Potentials inside a p-n junction [36]. The x-axis for all these pictures is physical space axis normal to the contact plane.
(a): Donor (N_D) and acceptor (N_A) densities, local space charge.
(b): Electric field (ϵ) inside the semiconductor.
(c): Internal bias (gap) voltage (V_{bi}) created by the electric field in (b).
(d): Conduction and valence band energy (E_C, E_V) relative to Fermi energy E_F

If a p and n-doped semiconductor were to make contact, near the contact plane all charge carriers of both sides would diffuse and recombine. Each majority charge carrier recombination leaves behind two unbalanced dopant site charges. The relative hole or electron concentration continues to decrease due to diffusion, and the area vacated of any free charge carriers extends. This process of diffusion continues, until the electric field created by the site charges counteracts the diffusion. This is the pn-junction equilibrium state. The space charge built up by this process inhibits the diffusion of carriers into the opposing side. This creates the depletion region, clearly marked in 13(a), the size of which can be calculated [29] using the formulas for the n-side width:

$$W_n = \left[\frac{2K_s\epsilon_0}{e}\frac{n_A}{n_D\left(n_A+n_D\right)}V_{bi}\right]^{1/2}. \tag{8}$$

K_s: Dielectric constant, for silicon 11.8 [29].
ϵ_0: Vacuum electric permittivity, $8.854 \times 10^{-12}\,\mathrm{F\,m^{-1}}$ [37].
$n_{D/A}$: Donor / Acceptor densities.
V_{bi}: Built-in bias voltage (see equation 11).
W_n: Width of the pn-junction's n-side.

The p-side width can be analogously computed. It can be expressed as the n-side width multiplied by the ratio of doping densities, as total leftover ion count numbers must be equal within the depletion region.

$$W_p = \frac{n_D W_n}{n_A} = \left[\frac{2K_s\epsilon_0}{e}\frac{n_D}{n_A\left(n_A+n_D\right)}V_{bi}\right]^{1/2} \tag{9}$$

Doping densities can range between multiple orders of magnitude in concentration. Having the two formulas above in mind, one can engineer p-n junction depletion regions to be greatly imbalanced in their reach inside the n or p material. Now we can add these two ranges to get the total width.

$$W = W_n + W_p = \left[\frac{2K_s\epsilon_0}{e}\left(\frac{n_A+n_D}{n_A n_D}\right)V_{bi}\right]^{1/2}. \tag{10}$$

The p-n junction in its equilibrium state has the potential barrier V_{bi} and is not conductive for small voltages. This built-in potential can be calculated using [29]

$$V_{bi} = \frac{k_B T}{e} ln\left(\frac{n_A n_D}{n_i^2}\right). \tag{11}$$

If one applies an external potential difference, it depends on the resulting electric field what the total current through the junction will be.
If the electric field is applied from left to right [4] in figure 12, electrons from the n-type are pulled to the right side, and holes in the p-type are pulled to the left side. Since both majority charge carriers are drawn away from the depletion region, the depletion region is enlarged. This matter follows a slightly adapted relation of formula 10 [29]:

$$W = \left[\frac{2K_s\epsilon_0}{e}\left(\frac{n_A+n_D}{n_A n_D}\right)\left(V_{bi}+V_{ext}\right)\right]^{1/2}. \tag{12}$$

A characteristic curve for a silicon diode is shown in figure 14. This makes it easy to understand the current response of a diode depending on the applied outer voltage difference. For negative voltage applied, the depletion region

[4] Conventional current would flow from left to right, electrons from right to left

extends, as the outer electric field adds to the internal one. Because charge carriers need to cross the depletion region in order to conduct current through it, ideally no current can flow in this configuration. This external negative voltage is called reverse bias.
Since the pn-junction forms two conductive areas separated by a layer that is not passable for electrons, a reverse-biased pn-junction forms a capacitor. The voltage on this capacitor varies the depletion region depth, and thus its capacitance. This relation is expressed by the formula [29]:

$$C_J = \frac{K_s \epsilon_0 A}{W} \tag{13}$$

C_J: Junction capacitance.
K_s: Silicon dielectric constant 11.8 [29].
ϵ_0: Vacuum electric permittivity, $8.854 \times 10^{-12}\,\mathrm{F\,m^{-1}}$ [37].
A: Diode junction area.
W: Width of the depletion region.

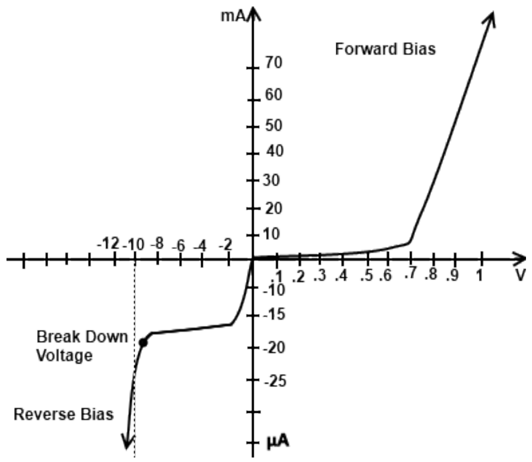

Figure 14: Characteristic current-voltage (IV) curve for a silicon diode [38] (modified).

The other case is called forward bias. Here, both majority charge carriers are pushed towards the depletion region. If the voltage is large enough to push them over the potential barrier created by the space charge in the depletion region, they will recombine with their counterparts and current will flow.

For the purpose of detecting ionizing particles, a pn-junction plays a central part. Ionizing radiation passing through a semiconductor will excite and ionize some lattice electrons and locally create an excess of charge carriers. These will diffuse to lower concentrations. They can also recombine over time with other minority charge carriers.

Since electrons have higher mobility than holes, they contribute most to signal creation [32]. For a signal to be created, these charges need to be moved to create a current, which can be measured. If the particle passed through the p-region of a semiconductor outside the depletion region, the excited electrons can diffuse towards it. If they reach the depletion region, they are accelerated by its electric field and drift to the opposing side. Upon reaching the other side of the diode, the charges have been successfully separated. This is because the holes will not diffuse through the equilibrium state depletion region. For this reason, a depletion region is central to a semiconductor particle detector. With correct implementation of a reverse bias, the depletion region can be extended. If used for detection purposes, the charge transport balance shifts now from the slow isotropic diffusion to faster directed drift, which makes the detector more efficient.

3.2 ALice PIxel DEtector

The ALPIDE chip is a sensor realized in the 180 nm CMOS process. CMOS stands for Complementary Metal Oxide Semiconductor. This process is known for enabling usage of both n- and p-wells, thus making pnp and npn transistors on the same dye a reality. Eliminating the need for any pure npn or pnp technology to be realized using pull-down or pull-up transistors, makes CMOS logic only consume power when in the process of switching from one to another state. For this reason CMOS technology is known to be very power saving.

The ALPIDE chip measures 15 mm × 30 mm. It consists of 512 × 1024 pixels, each 26.88 µm × 29.24 µm large [39]. The readout and control section is 1.2 mm × 30 mm large and located adjacent to the 512th row of pixels, on the bottom of figure 15. On the rim at the bottom side of the ALPIDE chip, there are bonding pads for interfacing with it from the outside. There are also pads on the pixel matrix, used for bonding in staves used in ITS2. For all purposes pertaining to beam tests and better control of the sensor, these peripheric bonds are used. Here wirebonds attach to die pads and connect it to an outer PCB, called the carrier card, used to readout and process data.

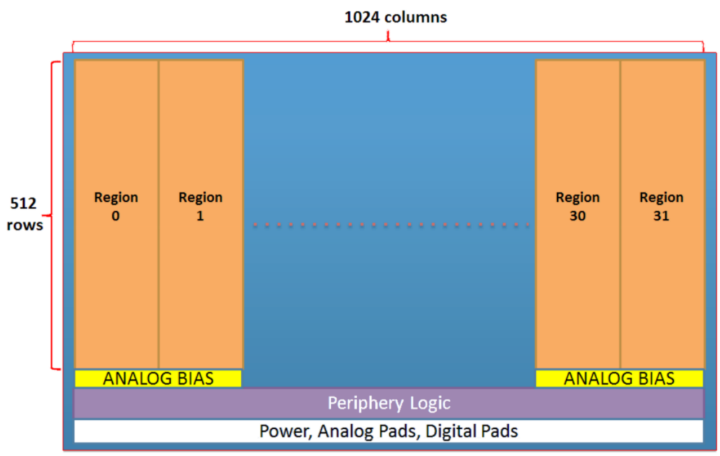

Figure 15: Layout of the ALPIDE chip, on the top left is pixel (0,0). The wirebonds attach from the bottom. [39]

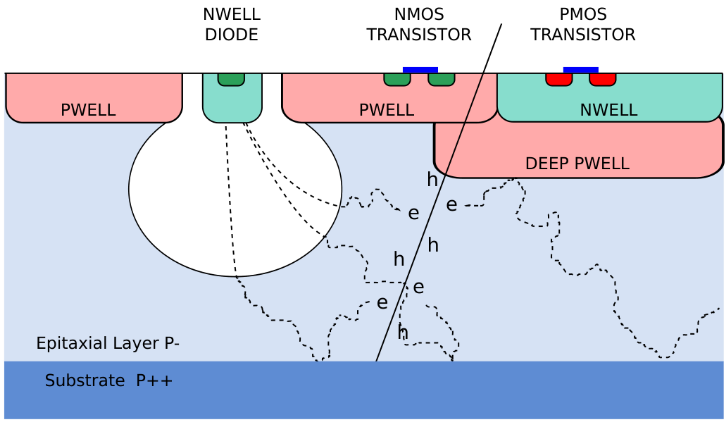

Figure 16: A stylized ALPIDE pixel depletion region cross-section [13].

The central part of each pixel is the collection diode. It is visible to the left in figure 16. The epitaxial layer is its low p-doped side. The diode n-side is only about 2 µm in diameter [39]. Due to the large doping difference from the higher doped n-side to the lower doped p-type epitaxial layer, the depletion region is greatly asymmetrical. It extends far into the epitaxial layer, and can be further extended by applying a reverse bias voltage between the substrate and analog ground.

When an ionizing particle traverses the detector, it will travel through the 25 µm thick epitaxial layer as well. Doing this it will create electron-hole pairs in a channel along its flight path. These are majority charge carriers and will diffuse to lower concentrations. If the electrons that have been freed in the epitaxial layer pass into the depletion region, they get collected in the highly-doped n-well of the collection diode. They therefore lower the n-well potential by a few tens of mV, which is picked up [39]. From there, this analog signal is amplified and shaped. The signal is discriminated with a global comparison threshold and thereby digitized. The following digital section of each pixel includes three hit storage registers, a register for masking and pulser logic.

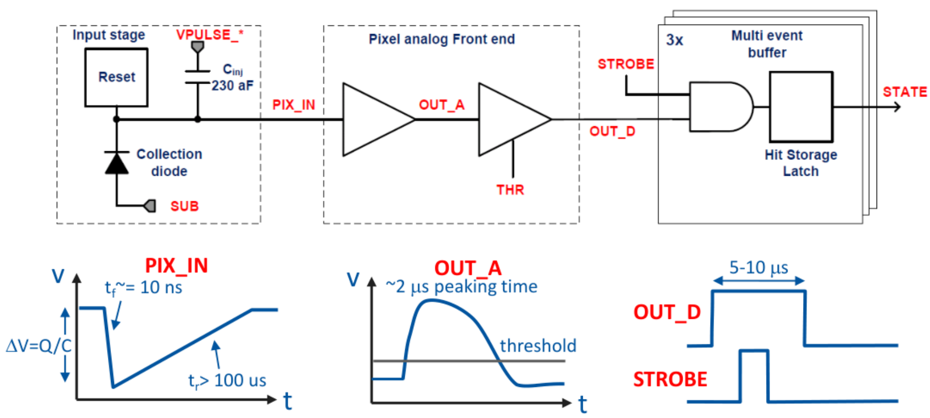

Figure 17: Block diagram of the ALPIDE pixel cell [39].

A pixel hit is stored in the multi event buffer, if the pixel receives a global STROBE signal, and the discriminator is above threshold. Three STROBE signals are generated when an external TRIGGER signal is supplied to the chip. Alternatively, the chip can be operated in internal mode where STROBEs are initiated by an internal sequencer. The entire signalling process flow can be seen in a greatly summarized version in figure 17. From the collection diode in the left box, via the analog front-end in the center box, to the right box where the digital part is simplified. Below, the respective signal shapes present at the input or output are qualitatively drawn.

For testing purposes, each pixel has its own pulse injection capacitor [5]. It is used to inject a test charge into the pixel front end.

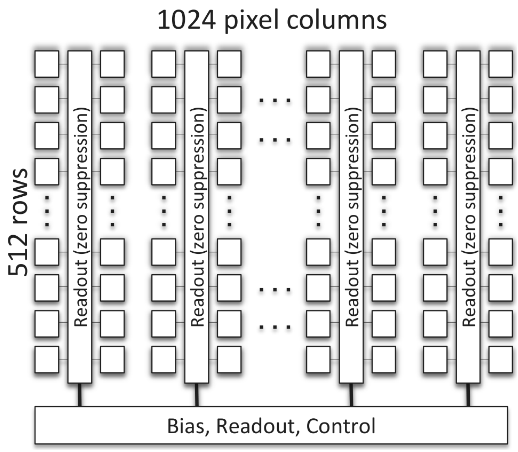

Figure 18: General architecture of the ALPIDE chip [39].

Each pixel column is grouped with another one to form in total 512 double columns. Each double column has its own Priority Encoder, a circuit that handles total Input/Output tasks of its assigned 1024 pixels. This refers to buffering of data as well as distribution of readout and configuration signals to the pixels [39].
This layout can be seen in figure 18, the priority encoder is located between two pixel columns.
Pixel hit data is read out from the in-pixel buffers by the responsible Priority Encoder. It supplies the periphery with the address of a hit pixel, and resets the memory element of that particular pixel. This cycle repeats until all pixels with valid hit information have been read out and transmitted. Because only hit pixels are communicated, the readout from pixel matrix to periphery is zero-suppressed.

The entire matrix is divided into 32 regions, each one consisting of 16 double columns. Each region has its own Region Readout Unit in the periphery. All regions are read in parallel, while the 16 Priority Encoders are addressed sequentially.

[5] C_{inj}, in figure 17 top left.

Whenever digital and analog sections are operated together, there is a need for translating signals between the two. These translators are called analog-to-digital (ADC) converters or digital-to-analog (DAC) converters, for the reverse direction.
The chip periphery section contains 13 8-bit DACs. Of these, 11 are required for supplying pixel front-end analog reference signals such as setting threshold and tuning signal shaping. A 10-bit dynamic range ADC provides digital readout of supply voltages, a temperature sensor and a band gap voltage reference. It can also be used to test the internal DACs.
ALPIDE chips are tested on-wafer and classified into 4 categories according to their quality. From high quality with no major faulty circuits in descending order: Gold, Silver, Bronze and NOK (not OK). Classification variables include bad pixels and power consumption in analog and digital domains among other criteria.
ALPIDEs are also tested after bonding to ensure they remain functional and to identify potential problems. The DAC test scan is part of the ALPIDE testing procedure to verify that newly produced and bonded chips have functional digital to analog converters. In it, digital values spanning the 8-bit range of the DACs are sent to each DAC input. The output analog signal is then converted back to a digital number using the ADC, and stored to file. In the resulting plot (figure 19) the two data spaces are clearly visible. The $2^8 = 256$ settings for the DACs on the x-axis, with $2^{10} = 1024$ entries for the ADC on the y-axis. The DACs responsible for current control have a shallower incline. This is not due to them occupying a different address space, but rather an internal scaling due to the nature of measuring current through a resistance.

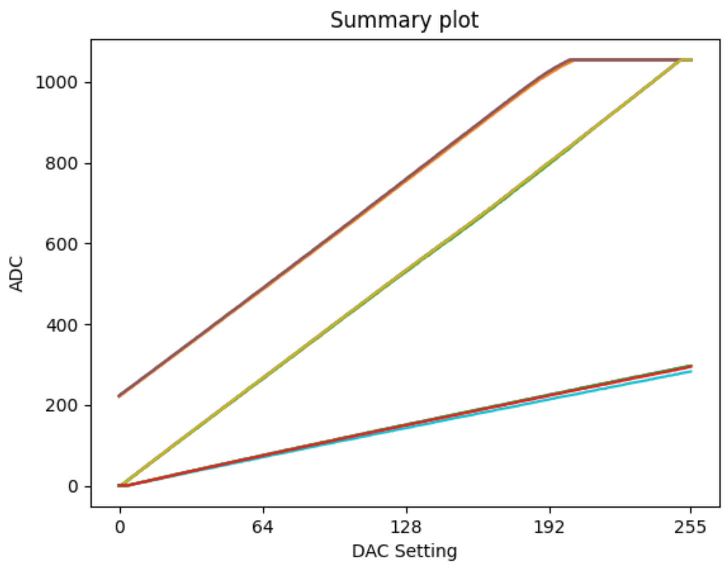

Figure 19: Nominal DAC-scan done on chip T847786 W19 BC4 on 2022-07-21.

The next part of the ALPIDE test procedure is the pulsing of the analog and digital pixel domains. This is done in order to test them for electrical

responsiveness.
The central piece of a chip test is the threshold scan. Here, each pixel has a specified amount of charge injected in its front-end.

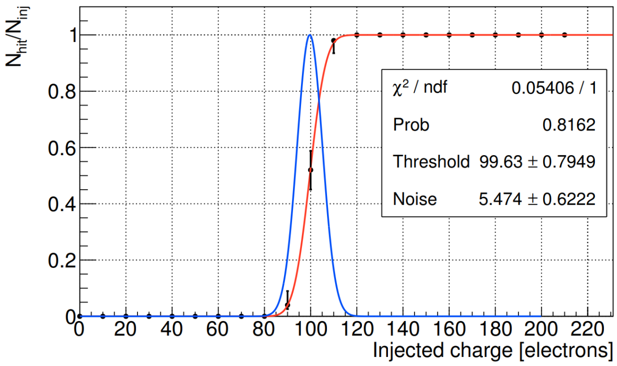

Figure 20: Quotient of hits and total injects (N_{hit}/N_{inj}) into a pixel, plotted against the injected charge (Q_{inj}). The charge which causes a pixel response with 50% probability is called the threshold. The blue curve is the derivative of the red one, the standard deviation of which represents the electronic pixel noise [40].

The amount is varied and injected multiple times in order to build some statistics of pixel responses relative to pulse strength. During this test the pixel responses are saved. One result is shown in figure 20. This figure is only regarding one pixel, but performing such a test on every pixel helps build a comprehensive summary picture of the entire chip performance.

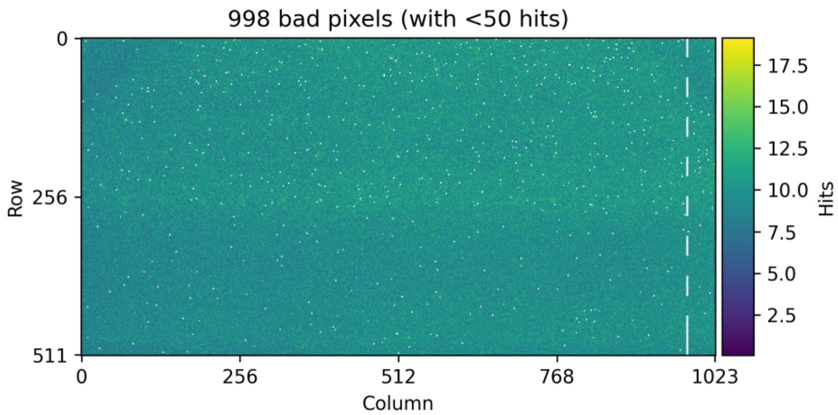

Figure 21: Example threshold scan over the chip area. White colored pixels mean that they did not respond to signals induced by the testing circuitry. The vertical white lines on the right are signs of faulty double columns, which is a common mode of failure for chips classified as bronze.

One such picture is figure 21. In it, one can see a half-failed double column to the right and a few non-responsive pixels all over the matrix. Slightly lower thresholds on the top corners can be observed due to the glue used to fix the ALPIDE chip on the carrier card. The relatively even color of the picture suggests that there are no local threshold anomalies present, due to for example radiation damage effects.

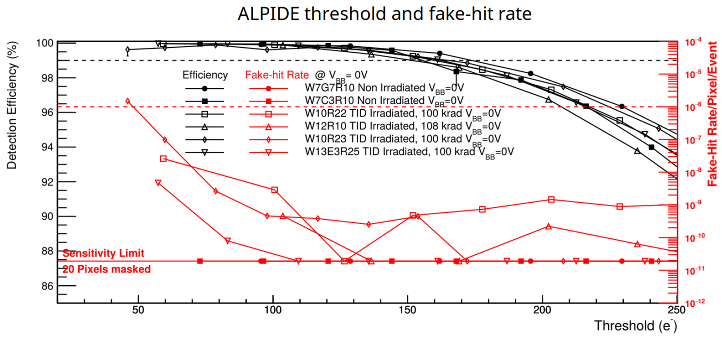

Figure 22: Different ALPIDE efficiencies (black) and fake-hit rates (red) vs. threshold at 0 V back bias [40].

The threshold needs to be tuned to allow for high detection efficiency, but also limiting the fake-hit rate, caused by noise in the sensor. This trade-off behavior can be observed in figure 22.
If the threshold has been tuned to 100 electrons, ALPIDE is over 99.98 % efficient 5, while keeping the fake hit rate way below the 10^6 target of the technical design report [13].

3.3 Accelerators and beam tests

To test detectors in a more realistic environment than a lab, one can use a beam test facility with a particle accelerator. They provide a high degree of control over parameters such as particle momentum, particle beam size, divergence and more. In most beam tests high energy particles are measured. This is done to minimize scattering to be able to improve the accuracy of parameters of interest of sensors. Such parameters are for example: position resolution, time resolution, efficiency and effects of radiation damage.

Utilizing a structure called a beam telescope, the performance of a detector can be evaluated. Telescopes are a sequence of particle detectors stacked one behind the other in the path of beam particles, so that a particle beam can be shot through all detectors. A single detector inside a telescope is also called a plane. When a particle passes through the telescope, ideally all planes register a hit. These hits are then combined to form a track, thus reconstructing the path a particle took through the telescope.

In general, in the center of the beam telescope another detector is placed for performance evaluation purposes. This special role detector in the center of the telescope is called a DUT, or device under test. Planes before and after the DUT are called reference planes, because they have a well known behavior and are able to record hits from particles with high efficiency, allowing for track reconstruction. Then, the tracks can be extrapolated to a point of interest on the DUT. Using the known characteristics of the detectors in the reference plane, the DUT can be characterized. For example the efficiency can be calculated when interpolating the intersection position from reference tracks onto the DUT. If the DUT has not registered a hit around the specified position, it was inefficient with respect to this track.

3.3.1 COSY at Jülich

COSY (Cooler Synchrotron) is a particle accelerator located in Germany. It has a circumference of 184 m. The complex can accelerate protons up to 2.7 GeV/c, and deuterons up to 2.1 GeV/c [41]. It consists of a primary accelerator in the shape of a cyclotron, a main accelerator and cooler ring, and three final experimental caverns.

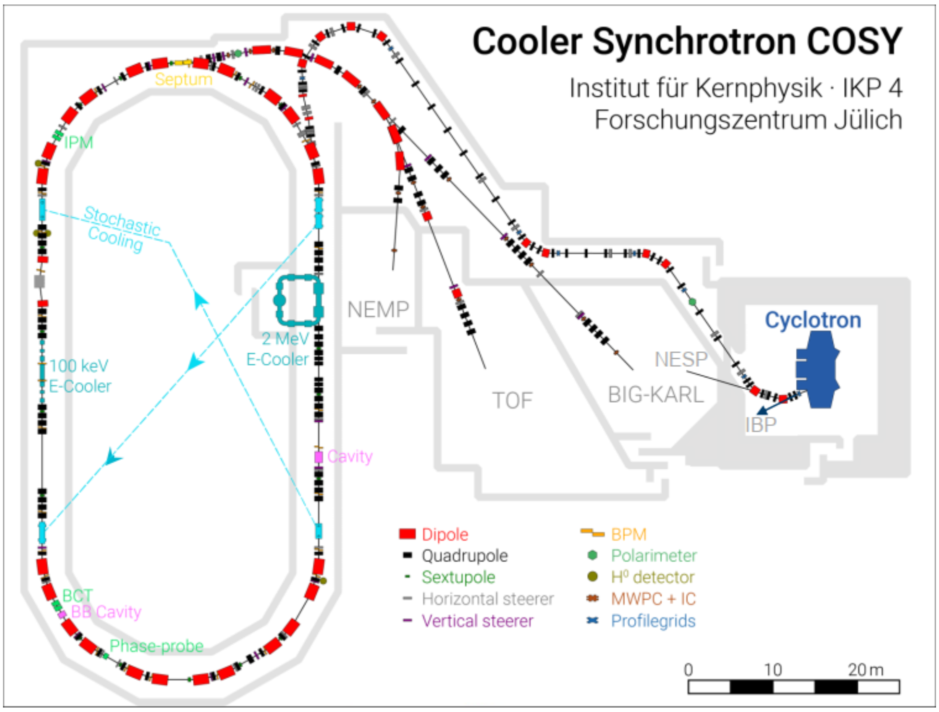

Figure 23: COSY layout pictogram [41]. Deuteron data for this thesis was gathered in the cavern named *NEMP*.

The main feature of this accelerator is the possibility to provide deuterons. This capability was utilized to gather pure deuteron data which is rarely found in other beam facilities. Due to the design of COSY at Jülich, the kinetic energy of deuterons is limited. The maximum $\beta\gamma$ of the deuterons available at COSY can be calculated using the equations for relativistic kinetic energy:

$$E^2 = (pc)^2 + \left(Mc^2\right)^2 . \tag{14}$$

and for $\beta\gamma$ with equation 2. Using 1.875 GeV as the deuteron rest mass [42], we get:

$$\beta\gamma = p/\left(Mc\right) = \sqrt{\left(E/\left(Mc^2\right)\right)^2 - 1} \approx 1.12. \tag{15}$$

Therefore, the momentum of deuterons at COSY is not high enough to act as minimum ionizing particles, which range approximately $\beta\gamma = 3$ to 4. This results in a larger signal in the used detectors due to a higher amount of energy lost. Additionally, as scattering scales with $1/(p\beta)$ the scattering rate is higher compared to a minimum ionizing particle [15].

4 Simulation of cluster size in an ALPIDE

The goal of this work is to get a deeper understanding of the clustering behavior of the ALPIDE chip. Therefore, a theoretical calculation of real data analysis results would be preferable. In this section cluster sizes are studied using a simple simulation, following the explanations from [43, 44].

4.1 Mean energy loss in an ALPIDE

A charged particle traversing an ALPIDE loses energy by ionization according to the Bethe-Bloch equation 1. Since all particles considered in this analysis are at energies reasonably close to MIP level, the density effect correction can be ignored [25]. Since dopants have very little influence on the overall material density, using the density of pure silicon and the thickness of the epitaxial layer as 25 µm [45], for calculating the energy loss of a minimum ionizing electron in an ALPIDE epitaxial layer is justified. Energy loss in thin silicon layers cannot be accurately described by the Bethe-Bloch equation. This is because the Bethe-Bloch equation describes only the average energy loss, which as a result of the central limit theorem fits the energy loss measured in sensors with an active region thicker than 300 µm. This is why the Bichsel distribution, which describes energy loss in thin absorbers more accurately needs to be used. It predicts a charge deposit of around $1.1\,\mathrm{MeV\,cm^2\,g^{-1}}$ for silicon with a thickness of an ALPIDE [15]. The average energy needed to create an electron-hole pair is 3.65 eV in silicon [46]. Using the above numbers and silicon properties found at [47], the most probable amount of created electron-hole pairs is $60\,\mathrm{µm^{-1}}$. This works out to about 1500 total free electrons in the epitaxial layer, assuming that the particle passed through it perpendicularly.

4.2 Charge transport simulation

The mechanisms of charge transport from ionization paths to the detection diode are explained in section 3.1.1. There are two main ways electrons are transported through the epitaxial layer. In the case of ALPIDE, the main process via which charges get shared between pixel diodes is diffusion. This is because diffusion isotropically spreads free charge carriers towards regions with a lower charge carrier density. To describe diffusion one needs characteristic values that describe the system.

The acceptor density in an ALPIDE epitaxial layer is about $10^{13}\,\mathrm{cm^{-3}}$ [45]. From figure 24 one can read off that unbound electrons in such a doped silicon crystal have a lifetime of approximately 700 µs, after which they recombine with holes. The diffusion length L_n is calculated with the average carrier lifetime τ_n and the tabulated diffusion coefficient D_n of about $36\,\mathrm{cm^2\,s^{-1}}$ as in [29]:

$$L_n = \sqrt{D_n \tau_n}. \tag{16}$$

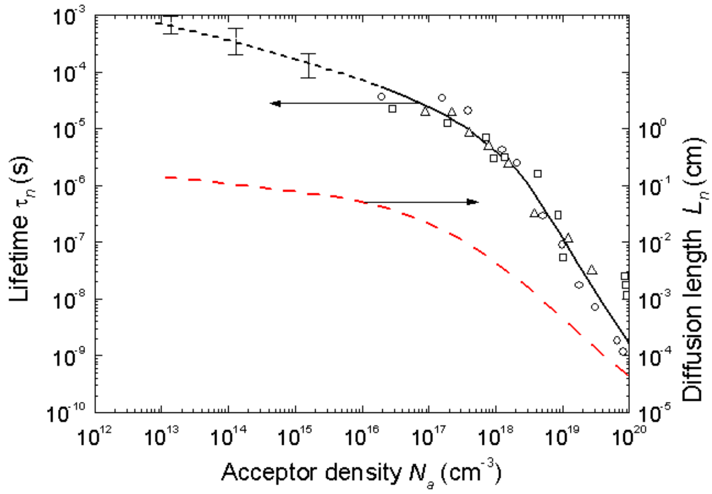

Figure 24: Average lifetime τ_n (black) and diffusion length L_n (red) for electrons vs. p-type doping density N_a. This plot is for silicon free of other contaminants at 300 K. [48].

Figure 24 describes pure silicon, which is why D_n is lower for the doped ALPIDE sensor. Nevertheless, for the purposes of a simple simulation, taking an approximate value is sufficient. For the diffusion length a value of 1 cm is chosen.

When electrons reach the depletion region generated by the collection diode of a pixel, they are subject to an electric field and drift and get collected at the deep nwell. The mobility of electrons at $1360\,\mathrm{cm^2\,V^{-1}\,s^{-1}}$ indicates that any drift processes in the ALPIDE epitaxial layer is completed within a time interval of the order of 1 ns. The carrier lifetime is significantly longer than this timescale, thus recombination does not lead to significant free charge carrier losses while drifting. Therefore, a simulation of charge transport can concentrate its efforts to describing diffusion and drift separately.

Because drift is always directed along electric field lines, the end points of any electron trajectory can be determined. This makes the statistic calculation of drift destinations irrelevant as compared to diffusion.
Hence, the focus of this work is the simulation of diffusion. Clustering is achieved mostly via the diffusion of majority charge carriers to other pixel diodes. To simulate this process, suitable models need to be selected.

The most straightforward method is implementing a random walk simulation along a discrete lattice. However, this implementation has the issue that not only large amounts of data needs to be computed, but a minuscule amount of information is accessed at the end, making it a very inefficient calculation. The exact path of the electrons in the epitaxial layer is not of importance here. The only result of interest is the end point of the electron travel path, or better, the collection diode within which pixel it hit. Then all the electrons that hit a specific diode can be counted, and compared with the discriminator threshold to determine if a hit is registered. If the collected charge at the collection diode surpasses the pixel discriminator threshold, the pixel registers a hit.

The time it takes for electrons of an ionization channel to diffuse all the way to the collection diode can be estimated. Using a diffusion coefficient of $\approx 36\,\mathrm{cm}^2\,\mathrm{s}^{-1}$ [32] for calculation, the time is in the order of 170 ns.
In the ALPIDE manual [39], a peaking time of ≈ 10 ns is given for the front-end diode signal. This signal is discriminated, and a 10 µs pulse is asserted [39]. This signal handling is significantly longer than the diffusion time and thus is can be assumed that all charges freed in the ionization channel have either recombined or have been collected by the diode.

The recombination process causes electrons to recombine with holes, effectively removing them as free charge carriers. This means that the diffusion model needs to incorporate the recombination of charge carriers. This will decrease the signal contribution exponentially with the travelled distance through the epitaxial layer, as seen in equation 17.

$$P_r = e^{-\frac{r}{L_n}}; L_n = \frac{r_{\frac{1}{2}}}{\ln(2)} \tag{17}$$

r: Traveled distance of the particle.
$\mathrm{r}_{\frac{1}{2}}$: Distance after which half the free charge carriers have recombined.
$\mathrm{L_n}$: Exponential decay factor, distance after which 1/e of all free charge carriers have not recombined. Also called attenuation length λ.
$\mathrm{P_r}$: Probability of a particle arriving at distance r.

As seen in figure 24, this material variable L_n is strongly dependent on the material purity. In pure and undoped silicon the diffusion length is in the order of millimeters, but it decreases significantly as doping concentrations increase. Since doping profiles of the ALPIDE sensor are classified, the value for the diffusion length can only be estimated. As discussed above in section 4.2, a value of 1 mm is determined for this simulation.

Since diffusion is isotropic, it can be described as an effective flow of electrons from high to low concentrations of equally charged carriers. Exploiting the rotational symmetry, it can be assumed that the electron density distribution is equal on the surface of a sphere. Assuming a center point P and point on the detector surface M, we can define a radius vector $\vec{R}$, as illustrated in figure 25a. This sphere defined by the radius $\vec{R}$ has a surface area equal to $4\pi|\vec{R}|^2$.
The probability that a diffusing electron from point P reaches M is then described by

$$\rho\left(\vec{R}\right) \mathrm{d}\phi \mathrm{d}r = \frac{\mathrm{d}\Omega|\vec{R}|^2}{4\pi|\vec{R}|^2} \exp\left(-\frac{|\vec{R}|}{L_n}\right) = \frac{\mathrm{d}\Omega}{4\pi} \exp\left(-\frac{|\vec{R}|}{L_n}\right) \tag{18}$$

With $\mathrm{d}\Omega$ being the infinitesimal solid angle element, which is shown in figure 25b. Considering spherical coordinates with the azimuth angle ϕ and the

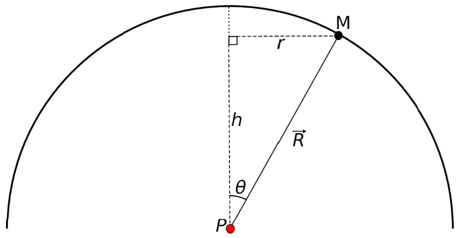

(a) Graphical representation of the geometrical part of the charge diffusion model.

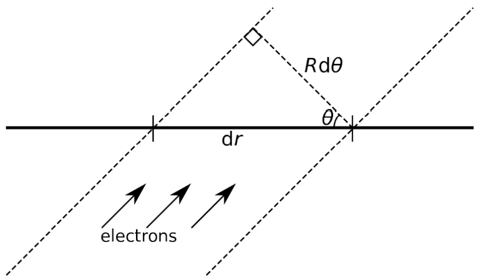

(b) Infinitesimal view at point M.

Figure 25: Electrons diffuse isotropically and their density is equal on the surface of the sphere in (a). Small r is the scalar projection of $\vec{PM} = \vec{R}$ on the detection surface [44].

polar angle θ as illustrated in figure 25b, we can realize from the area element for the solid angle $\mathrm{d}\Omega = \mathrm{d}\theta\mathrm{d}\phi\sin\theta$. From the figure 25b the following relation can be derived: $\mathrm{d}\theta = \left(\cos\theta/|\vec{R}|\right)$. Inserting these found geometric terms in equation 18 results in

$$\frac{\mathrm{d}\Omega}{4\pi}\exp\left(-\frac{|\vec{R}|}{L_n}\right) = \frac{\mathrm{d}\theta\mathrm{d}\phi\sin\theta}{4\pi}\exp\left(-\frac{|\vec{R}|}{L_n}\right) = \frac{\mathrm{d}r\mathrm{d}\phi}{4\pi}\frac{hr}{|\vec{R}|^3}\exp\left(-\frac{|\vec{R}|}{L_n}\right). \tag{19}$$

Where the equation has now been transformed into spherical coordinates, such that the natural geometry of the ionization channel along a particle path is reflected. The vertical (z-, $\theta = 0$-) axis is defined along h-direction, which is also along the particle flight path, normal to the detection surface. Because the sensor surface is a rectangle in Cartesian coordinates, the integrand can be further transformed to Cartesian coordinates with $\mathrm{d}r = \mathrm{d}x$ and $r\mathrm{d}\phi = \mathrm{d}y$ from the Jacobi-matrix. Substituting this in equation 19, the result is [43, 44]:

$$\rho\left(\vec{R}\right)\mathrm{d}x\mathrm{d}y = \frac{h}{4\pi|\vec{R}^3|}\exp\left(-\frac{|\vec{R}|}{L_n}\right)\mathrm{d}x\mathrm{d}y. \tag{20}$$

ρ: Probability of one electron reaching until $\vec{R}$.
h: Electron depth under the detection surface.
$\vec{R}$: Vector from the electron starting point P to point on the detection surface M.
r: Scalar projection of $\vec{R}$ onto the detection surface.

Here $\mathrm{d}x\mathrm{d}y$, represents a surface element on the top end of the epitaxial layer, where electrons are collected.
However, half of the electrons from the ionization have a direction travelling downwards i.e. towards the substrate. The substrate below the epitaxial layer is heavily p-doped, which results in a significant potential barrier at the interface with the epitaxial layer [43]. Electrons that diffuse and hit the

substrate are therefore reflected back into the epitaxial layer. Assuming that their incidence angle is equal to the corresponding reflection angle, this can be described by adding a second term to the diffusion model.

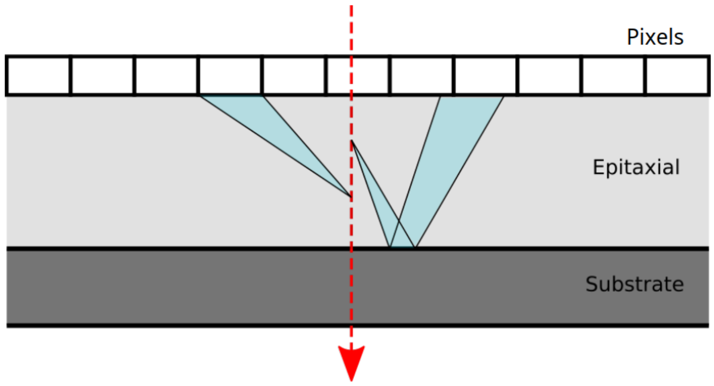

Figure 26: Pictogram of the diffusion model including reflection, not to scale. [44].

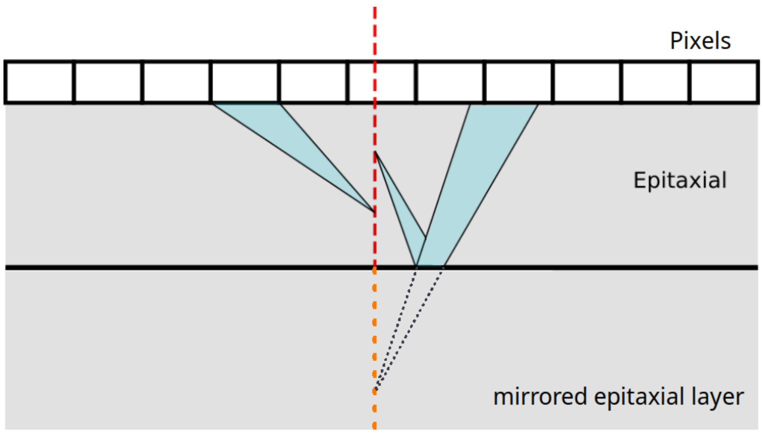

Figure 27: Visualization of the implementation of reflection on the epitaxial layer - substrate border, represented by the black horizontal line in the center. The reflection implementation is shown by the black dotted lines, that originate from behind the mirror plane. Modified from [44].

Since ideal reflections can be described by duplicating the system along the reflector surface, equation 20 can be transformed to match the geometry shown in figure 27. Only the electron diffusion depth h and the z-coordinate of the target point M is different for each of the two contributions. Taking l as the epitaxial layer thickness and using the transformation

$$h' = 2l - h; \;\; \vec{R}' = (x, y, h') \,, \tag{21}$$

in equation 20, the formula is adapted.
Figure 27 shows the complete implemented model in pictogram style. Two different diffusion angle paths for different pixels are shown.

The contribution from reflected electrons is about 20 % of the signal for the central pixel. This is because the average solid angle for reflected electrons hitting the same pixel is smaller than for electrons taking the direct path, as it can be seen in figure 27. The fraction can be obtained when computing the individual contributions of the different terms isolated from one another.

Adding both contributions, the total signal received by one pixel I is equal to the integral

$$I = \frac{1}{4\pi l}\int_{x_0}^{x_1}\int_{y_0}^{y_1}\int_{h=0}^{l}\frac{h}{(r+h)^{3/2}}\exp\left(-\frac{-\left(r^2+h^2\right)^{1/2}}{L_n}\right) + \frac{2l-h}{\left(r^2+(2l-h)^2\right)^{3/2}}\exp\left(-\frac{-\left(r^2+(2l-h)^2\right)^{1/2}}{L_n}\right)\mathrm{d}x\mathrm{d}y\mathrm{d}h. \tag{22}$$

The integration along the h-direction is constraint by the path length along the ionization channel in the epitaxial layer. The integration needs to be normalized to one over the epitaxial layer depth, l = 25 µm. The integration over h sets the passing particle trajectory perpendicular to the epitaxial layer surface. This is a good approximation since in the used real data the particle tracks hit the chip predominantly perpendicular with only negligible angular deviations of the order of 1 mrad.
The x-y-integration covers one entire pixel area. In reality the collection diode is comparatively small as compared to the pixel pitch, having a diameter of only 2 µm [39]. The model integrates over the full pixel surface, because the ALPIDE pixel is designed such that almost all charges generated in the ionization process are directed towards and collected at a pixel diode.

As a result of the diffusion length, the probability of electrons generated along the particle path and reaching the upper epitaxial layer surface is not unity, since the charge carriers can recombine. The integration result equals the average probability of a charge from anywhere along the ionization channel to hit in between the rectangle defined by (x_0, y_0) and (x_1, y_1). To account for different in pixel hit positions of the traversing particle the integration limits must be adjusted accordingly. For an exemplary particle hit in the center of the pixel the integration boundaries are $(x_0, y_0) = (-0.5 \cdot p_x, -0.5 \cdot p_y)$ and $(x_1, y_1) = (0.5 \cdot p_x, 0.5 \cdot p_y)$, where $(p_x, p_y) = (29.24\,\mu\text{m}, 26.88\,\mu\text{m})$ denote the respective pixel pitches. This way, the integration covers a rectangle with the origin in the center of the hit.

In order to get an absolute number of electrons collected in the considered pixel, the initial amount of charge $c = 60\,\mathrm{e}^-/\mu\mathrm{m}$ is multiplied with the resulting probability of the integration.

Upon finishing one integration step, the next integration step is done with a $\approx 0.054\,\mu\text{m}$ shift applied. This way, the entire pixel pitch is covered. For each subpixel location, neighboring pixel signals in a 5×5 pixel grid are calculated as well. It is then decided which pixels have accumulated enough charge to pass the set threshold, and the resulting cluster shape is saved for the result plot.

The computation can be made significantly faster when realizing that the model is axis-symmetric in x and y axes. Consequently, only one quarter pixel needs to be computed. The x- and y-axis is sampled with 544 and 500 steps respectively, in order to account for the different ALPIDE pixel pitch in these directions of 29.24 µm and 26.88 µm. These different substep counts must be introduced because the substep size needs to be equal in x and y direction, otherwise one axis is oversampled compared to the other.

$$\begin{aligned} \frac{29.24\,\mu\text{m}}{26.88\,\mu\text{m}} &= 1.0877976 \\ \frac{544}{500} &= 1.088. \end{aligned} \tag{23}$$

This results in an under/oversampling of either axis by just 0.02 %.
So far drift in the depletion region of the detection diode is completely neglected, in order to make the model simple enough to be implemented as a standard integration.
Since the diode depletion region catches most charges if the ionization path passes through it, these electrons do not undergo diffusion. The depletion region extends below the 2 µm large diode, with a droplet-like shape inside the epitaxial layer. If a back-bias voltage is applied, it extends even further and thus takes even more charges from diffusion. In this simulation it is therefore assumed that within a specific radius around the pixel center not enough particles undergo diffusion to get adjacent pixels above their threshold. This would result in a circular region centered on the pixel diode, where only single pixel clusters are produced. Since the electric fields in ALPIDE sensors are classified, the extent of such an area is largely speculative.

However, some efforts to calculate the approximate size of the depletion region can be made.
The approximate shape of the depletion region can be assumed to be spherical because of the very low concentrations of dopants in the epitaxial layer and the radial extent around the collection diode, as well as the deep n-wells. From figure 28 the resistivity of the epitaxial layer can be estimated for a doping concentration of $10^{13}\,\text{cm}^{-3}$ to be $\approx 1.6\,\text{k}\Omega\,\text{cm}$. The equation 10 for depletion region width can be simplified using $n_a + n_d \approx n_d$, since the donor part of the diode is orders of magnitude heavier doped. Substituting equation 6 for silicon resistivity into equation 10 we get the simpler formula 24 for the depletion region depth.

$$W = \sqrt{2K_s\epsilon_0\mu_p \cdot \rho \cdot V_{bias}} \tag{24}$$

The constants are given under equation 8. The total bias voltage is 3.8 V, as the diode is operated with −3 V reverse bias voltage, to which the internal gap voltage of 0.8 V at room temperature needs to be added. As a result

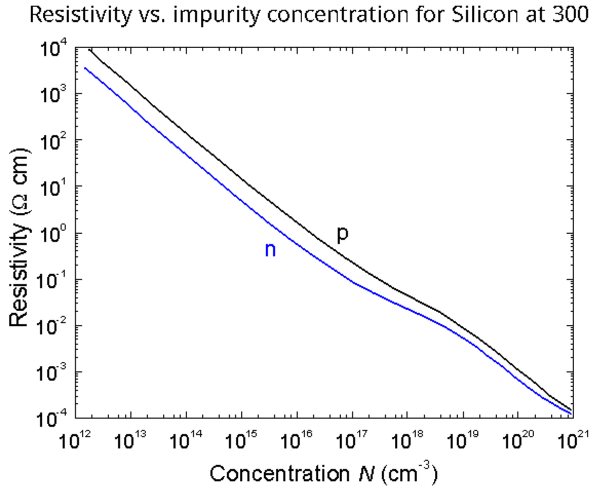

Figure 28: Silicon resistivity at 300 K depending on impurity concentration and type [48]. The hole mobility at this temperature is $460\,\mathrm{cm^2\,V^{-1}\,s}$.

the depth of the straight depletion region is estimated at 970 µm. This is however assuming the simple depletion region shape of a cuboid, where both n- and p-side have the same cross-section. Inside the epitaxial layer however, the depletion region is spherical. This approximation can be used with the geometry of the diode n-well as an octagonal shape with 2 µm diameter [39] to calculate the radius of a sphere with the equivalent volume. This sphere would have a radius of 9 µm.
Another way to estimate the extent of the depletion region is via the internal geometries of one ALPIDE pixel as seen in [49] figure 1. The 2 µm large diode nwell is spaced from the electronics pwell implant by 3 µm. This together with highly doped deep p-wells shapes the depletion region in a sack-like structure extending into the epitaxial layer. This region will grow larger and deeper with growing back bias voltage. The entire depletion region covers about 5 % to 10 % of the total epitaxial layer volume when at a reverse bias of $-3\,\mathrm{V}$ [50]. Taking the mean value as an estimate, the volume of the epitaxial layer can be calculated to be $\approx 1470\,\mathrm{\mu m^3}$. Approximating the depletion region with a sphere with radius r, one can easily calculate from the volume of the depletion sphere a 7 µm radius.
The depletion region does not continue all the way to the substrate, but nevertheless will take some charge away that would otherwise diffuse to neighboring pixels. To account for this, the threshold can be shifted. The parameter choice of this simulation is obtained by matching the area of one pixel clusters between data shown in chapter 5 and simulation.

4.3 Results

The results of three simulations are plotted as 2D histograms on the left in figure 29. The axis ranges denote the pixel pitches in µm. The color corresponds to the cluster size that can be expected when a particle passes through that point on the pixel.

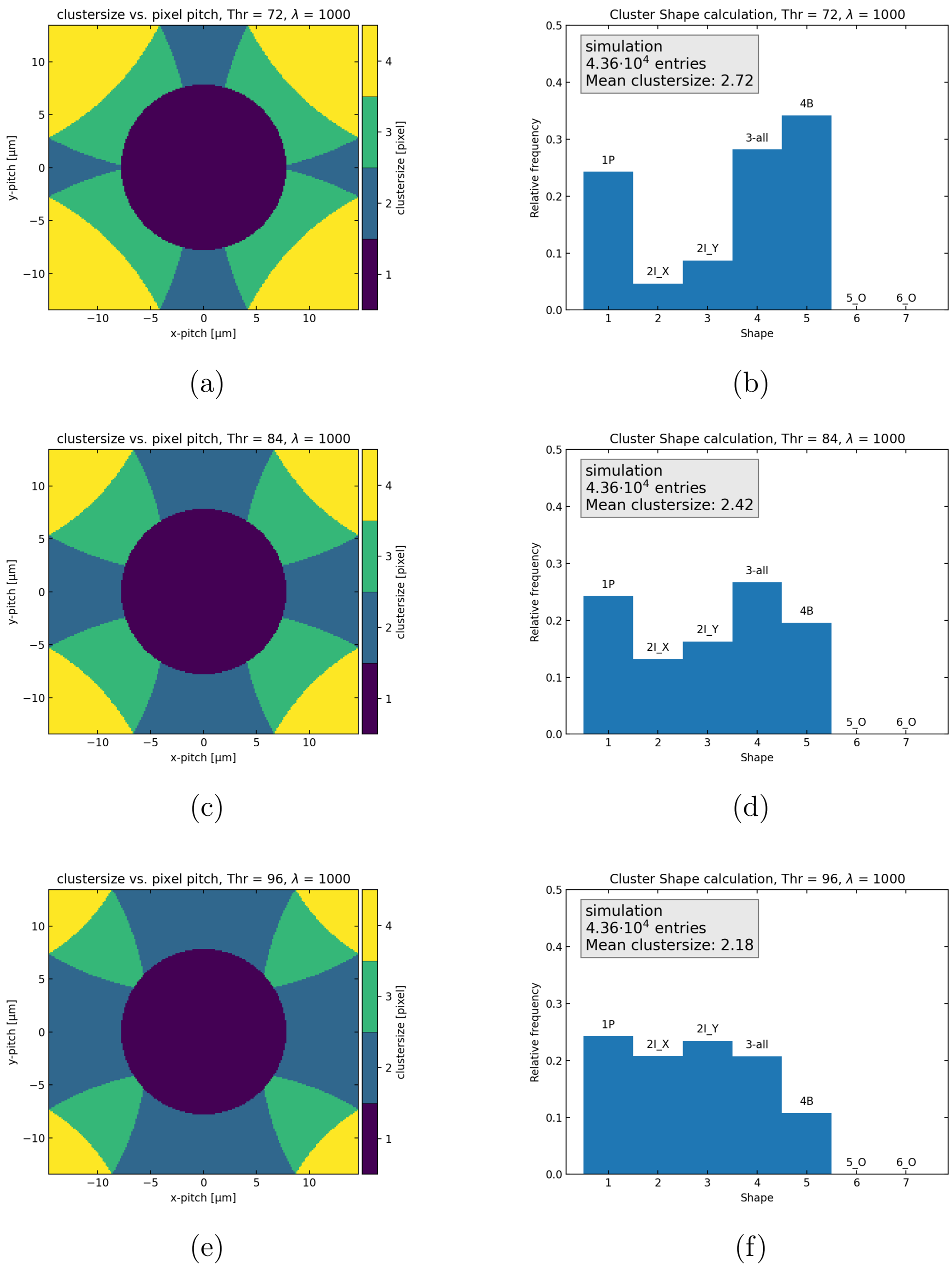

Figure 29: Cluster sizes relative to the point of incidence of a charged particle within one pixel and corresponding relative cluster shape frequencies for three different threshold values. The central radius here is fixed to 7.8 μm.

Additionally, the frequency distribution of cluster sizes and shapes is shown in figure 29 on the right side. The histogram bin labels hereby describe the cluster shapes as illustrated in figure 30.
For example '2X' cluster is a 2-pixel-cluster in X-direction.
In figure 29 three results are shown with the selected threshold increasing towards the bottom. The middle row hereby represents the best match as compared to the beam test data discussed in chapter 5. The figures in each row feature the same parameter settings.

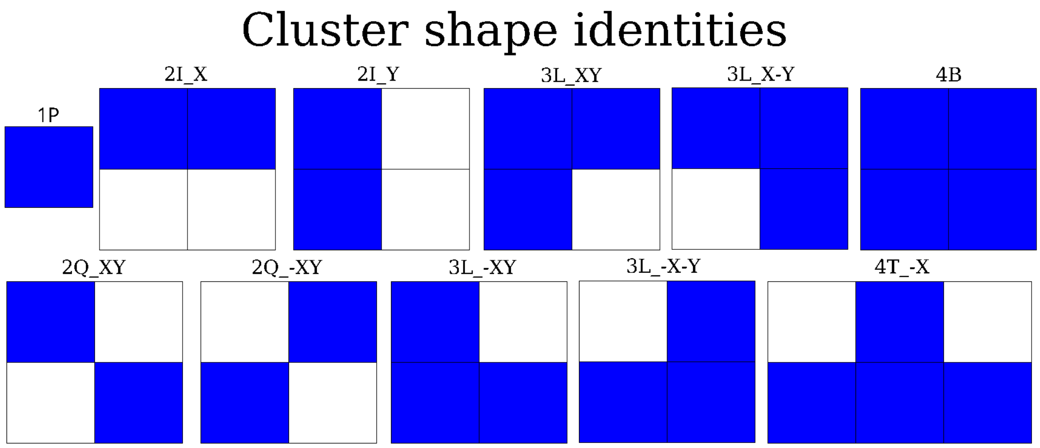

Figure 30: A lookup table for the major cluster shapes and their given names.

The visible areas defined by arcs indicating a predominant cluster size result from the contribution of neighboring pixels. The large circle in the center represents the influence of the center collection diode.
Tuning the variables to match the data has been carried out in the following: First, the relative frequency of cluster size one is fixed with the radius of the depletion region influence as described above. Secondly, the threshold is set to a value yielding the best match of the 4B-clustershape relative frequency to beam test data. The resulting value for the center circle is 7.8 µm, which is kept constant for all the plots in figure 29. The simulation in subfigures 29a and 29b are at lower threshold, and thus display a larger cluster size. Moreover, it can be seen that two pixel clusters are suppressed in favor of three and four pixel clusters, when the threshold is decreased. Figure 29e and 29f represent a simulation where the threshold was set higher and thus have decreased average cluster size.

Between the three figures, the cluster size distribution varies greatly. The average cluster size spans 2.18 to 2.72 pixels within a threshold range of only 22 electrons. With the set threshold being the only difference, it is clear that it plays a central role in determining the average cluster size.

Diffusion length has very limited impact in this context, since it is large as compared to the epitaxial layer thickness. Travelling 25 µm, a marginal 2.5 % of electrons with a diffusion length of 1 mm are lost due to recombination.
Generally, the cluster shape which has its two clusters arranged in x-direction is statistically preferred. When dividing the amount of x- and y-direction 2-pixel clusters, one gets a value of 1.23 corresponding to the setting shown in figure 29d. This is larger than the pure pitch asymmetry of 1.09. The reason is that the area where four-pixel clusters are produced is largely independent of the pitch asymmetry, and therefore reduces the area producing two-pixel clusters in both pitches equally, increasing the relative difference in length for the two.

5 ALPIDE hit cluster analysis

Datasets from beam tests or measurements with radioactive sources using an ALPIDE sensor can be analyzed to compare results to the model predictions described in the previous section 4.
In this section data corresponding to measurements with different particle species at different energies is analyzed and compared.

5.1 Experimental setup

An experimental setup comprising a so-called beam telescope is used for data taking. A beam telescope is shown in figure 31a. Single crucial components are described in the following.

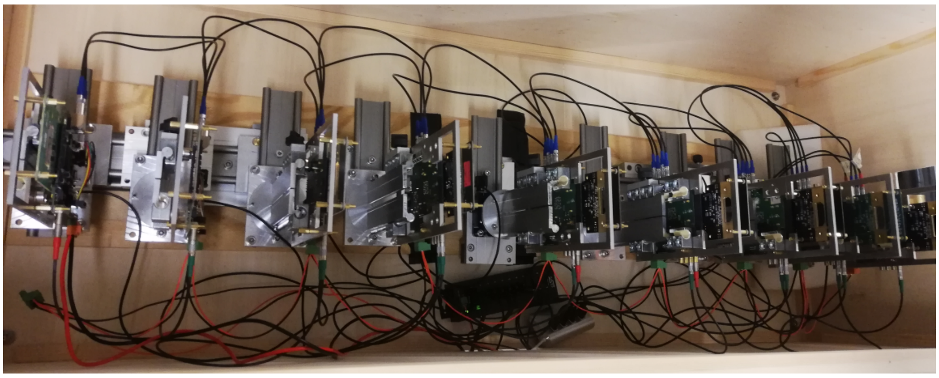

(a) Top-down view into a beam telescope inside a wooden box for light shielding.

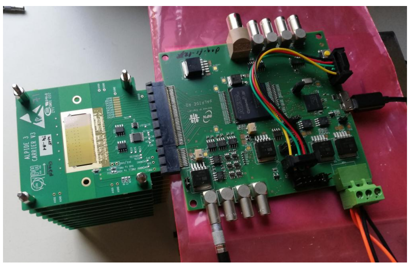

(b) Single ALPIDE chip with DAQ board.

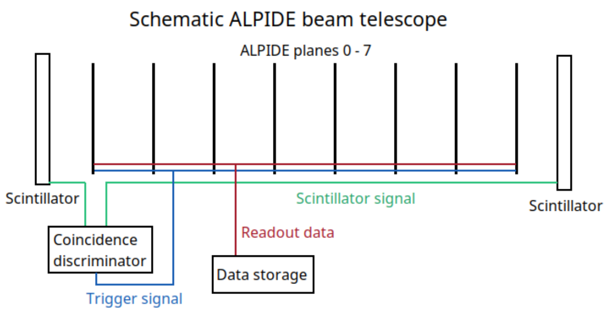

(c) Pictogram of an ALPIDE telescope setup.

Figure 31: ALPIDE telescope and detail view of an ALPIDE sensor bonded to its carrier card attached to a DAQ board. A setup similar to figure 31b was used to gather data from radioactive sources.

Data acquisition boards (DAQ) connect to ALPIDE sensors, which are bonded and glued to their carrier cards. They supply power and serve as the configuration and control infrastructure. This is a functional plane of which telescopes are built. The ALPIDE sensor and DAQ setup of two printed circuit boards is shown in figure 31b. The DAQ boards themselves are powered using an external power supply and connect via USB to a central computer, from which the chip is controlled and data is recorded during an experiment. Trigger signals provide a timestamp and mark the beginning of a recorded event. Within a time window after the trigger the chip hit data is read out and written to disk. A simple example of providing an external trigger signal is to use one scintillator in front or behind the telescope. Alternatively, two scintillators can sandwich the experimental setup with the ALPIDE sensors and their coincident and discriminated signals are used to trigger the read-out chain of the sensors. The latter trigger setup provides a more precise selection on particles which passed through the entire beam telescope. In both cases a trigger represents an event where at least one ionizing particle has passed through the telescope. As such, the analogue signal generated in the ALPIDE sensors are registered as hits, if the amount of deposited charge exceeds the set in-pixel discrimination threshold. Upon receiving a trigger signal, the DAQ boards read the pixel matrix hits from the ALPIDE sensors and send the data to the central computer. The data of individual sensors is received, merged into one event and stored using the EUDAQ2 software framework [51]. In order to cope with high event rates from the ALPIDE sensors, EUDAQ2 writes raw data files in a custom binary format.

To analyze these data files, the Corryvreckan software framework is used [52]. It is a modular beam test data analysis framework, which can be used to import the EUDAQ2 raw files containing ALPIDE hit data and perform a configurable analysis on it. There are dedicated Corryvreckan modules for specific tasks in the analysis chain. The main tasks used in this work are data reading, cluster building of hit pixels, reconstruction of particle tracks through the telescope and analysis of associated clusters from these tracks. As a starting point, Corryvreckan imports pixel hits from EUDAQ2 raw files and splits them into the original events.

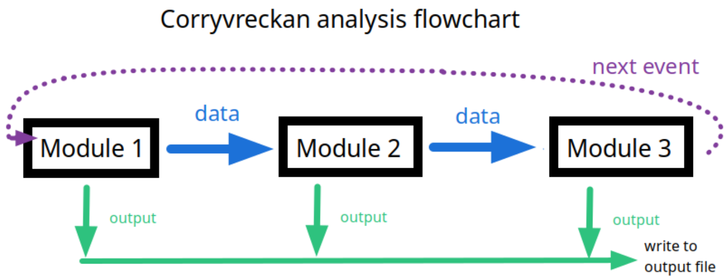

Figure 32: Corryvreckan internal program workflow

At each step in the analysis chain several result plots are produced and checks are performed. The Corryvreckan workflow is depicted in figure 32. Upon reaching the end of a raw file, all module outputs are written to a result file for further investigation and interpretation of the analysis results.

In typical analysis cases, a hitmap is generated in the beginning. This means that over a certain window of time or the whole dataset all registered pixel hits are plotted in a 2D-histogram. This is very useful for coarsely checking the integrity of read data since any malfunctioning pixels or dead areas on the chip would be visible. Data selection is important to exclude unwanted 'noise events' from data analysis and therefore minimize the contribution of

them to the final result. For this purpose pixels that fire more than 10 times more than the matrix average, are labeled as *hot*, get masked, and their signals are not used for further analysis steps.
Adjacent hit pixels within the same event are grouped into clusters. This is possible as the liberated charge deposited by a passing particle can cause a high enough signal in multiple pixels for them to register a hit due to charge sharing processes between the pixels 4.2. Adjacent in this context refers to touching neighbors, but not diagonal pixels. All hits farther apart than this will be considered as a separate cluster.
For tracking and other purposes where an exact point on the detector surface is needed for referencing, the geometrical center of the cluster is computed from the center points of the contributing pixels and saved as a property of the cluster.
The first step for an in-depth analysis is the software-based alignment, because the individual chips are never perfectly overlapping or parallel to one another due to limited mechanical precision of the experimental setup. Possible shifts of the sensors with respect to each other are accounted for in a geometry file, which defines the spatial topology of the telescope.
The first step towards a full alignment is called prealignment in Corryvreckan. It is based on correlation histograms in order to determine a shift of sensors with respect to a fixed plane. One pixel coordinate (row or column number) of one chip is correlated with the same coordinate of another hit from a different chip. The mean values of the obtained coordinate difference distributions is shifted to zero for each sensor plane. As such a preliminary alignment is realized.

A more precise method based on the information of reconstructed particle tracks can be applied subsequently to achieve a precise sensor alignment. This is achieved by iteratively translating and rotating individual sensors, such that the χ^2 - distribution of reconstructed particle tracks is minimized. Using a correctly aligned telescope, tracks can be efficiently reconstructed and saved.
Here, the χ^2-value is the sum of distances from the cluster positions and the corresponding fitted track positions divided by their respective error. A reduced χ^2-value (χ^2/nDoF) can be calculated when dividing χ^2 by the free parameters (called degrees of freedom) in the system. For example a straight line track is defined by four variables, which is the two-dimensional starting position and a two-dimensional slope. Each cluster provides two coordinates as the cluster position. The degrees of freedom for a seven plane setup as used in figure 33 are therefore ten (14 measurement points - four parameters of the straight line). In this figure several χ^2/nDoF distributions are shown for multiple alignment steps. Further steps do not improve the alignment any more, since a global minimum is achieved. Assuming a perfect fit i.e. the track model describes the data points exactly, a distribution peak at $\chi^2/\text{nDoF} = 1$ is expected.
In the case of our data, the track fit quality is considered sufficient, with a $\chi^2/\text{nDoF} = 1.14$ achieved after 2 iterations. This corresponds to an average

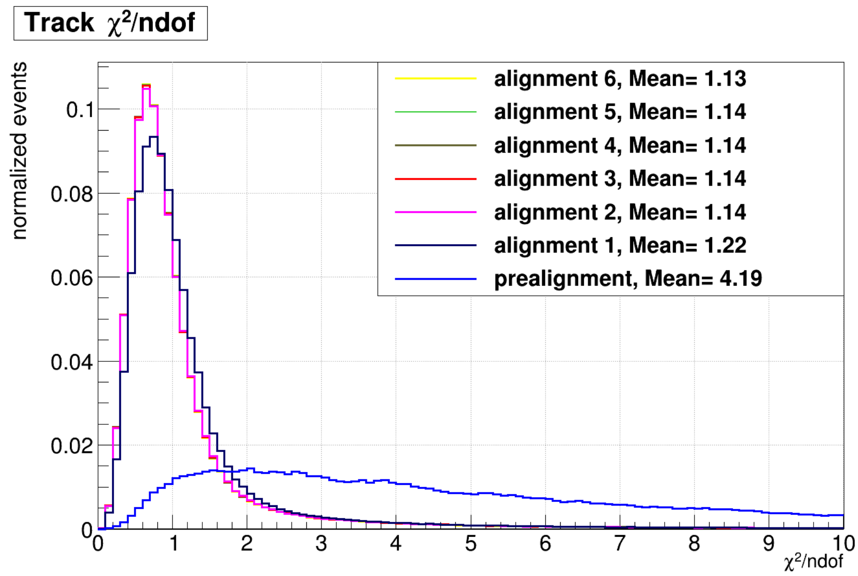

Figure 33: Track χ^2 per degree of freedom after repeated alignment steps. Two alignment steps already align the telescope well enough.

distance of 4.5 µm from cluster center to track per plane [53]. Given the ALPIDE pixel dimension, this allows for studying in-pixel effects. This is because the electron beam in this dataset has a momentum of 5.4 GeV/c ($\beta\gamma = 10\,500$). The scattering expected from one ALPIDE plane can be estimated using the Highland formula, an approximation for the width of the multiple scattering angular distribution as found in [15]:

$$\theta_0 = \frac{13.6\,\mathrm{MeV}}{\beta c p} z \sqrt{\frac{x}{X_0}} \left[1 + 0.038 \ln\left(\frac{x z^2}{X_0 \beta^2}\right)\right]. \tag{25}$$

θ_0: Sigma of the angular distribution.
p: Momentum of scattering particle.
z: Scatterer charge number.
x: Length of the traversed scatterer.
X_0: Radiation length of the scatterer.

Here, non-Gaussian tails in the scattering angle distribution are neglected, which correspond to 2 % of events featuring scattering to large angles [15]. The value given for the radiation length X_0 of silicon is 9.37 cm [47] and for dry air as 3.26×10^4 cm [54]. Given the sensor thickness as 50 µm and the distance between sensors as 2 cm, one can calculate the expected scattering, adding the two scattering angles in quadrature, which slightly underestimates the true value. In this case the result is 43.5 µrad, which is small considering this angle would cause a 0.87 µm displacement on the next chip in the telescope, which is less than the pixel size and implies that the effect of scattering in the whole telescope is limited to a quarter of a pixel pitch at most. For this reason scattering can be neglected and the usage of a straight line track model is justified.

But not all data used for this thesis is from particles that have this low

scattering effects. For the beam test at COSY deuterons with a maximum momentum of 1.4 GeV/c or approximately $\beta\gamma = 0.75$ where used. Also, electrons from a ^{60}Co beta-decay source are mostly at or below 318 keV/c decay momentum, with 0.12 % of decays happening with a momentum of 1.48 MeV/c [55].
^{241}Am emits alpha particles, with a momentum of 5.486 MeV/c (84.5 %), 5.442 MeV/c (13 %) and 5.388 MeV/c (1.6 %) [55].
Considering the rest mass of an alpha particle, the momentum from this decay is very low compared to the other considered particle sources. They have a range of only 43 µm in silicon [56], within which these alpha particles will deposit all their kinetic energy into the absorber material. Since alpha particles have trouble penetrating one ALPIDE alone, they are unsuited for a detailed comparison with simulation outputs.
For all mentioned particles at different energies, an analysis targeting cluster size and especially shape distributions is performed. Raw clusters and those associated to a reconstructed particle track are compared to investigate a difference in cluster shape frequencies. Finally, it is examined how clusters of different sizes are shaped.

5.2 Analysis of particle induced clusters

The cluster size analysis is performed using a dedicated custom Corryvreckan module. Additionally, the module responsible for cluster finding was modified to search for pixels two rows and columns apart from one another, to examine the possibility of clusters with one non-hit pixel in the middle. These might exist due to inefficiency. If the search window is too small, they would not be recognized as one cluster but rather two, of which one is not part of a track. Two pixels diagonally however is not checked, since here the radial distance is larger. For two pixel hits larger distances apart to be a single cluster, more pixels need to be inefficient in between the two pixels that registered a hit. Because pixels are proven to be very efficient in an ALPIDE sensor, multiple pixels not responding to a signal is statistically improbable.
A visualization of the area that is checked in the two clustering modules is given in figure 34. For a found hit, depicted as red pixel in the center of the picture, `ClusteringSpatial` checks all surrounding yellow pixels for additional hit pixels belonging to the cluster. If there are any new hits found, they are added to the cluster and iteratively checked with the same pattern next. The module `ClusteringSpatialExtra` adds the blue colored pixels to be checked for hits and potentially adding to the cluster.
For the main analysis, the module `AnalysisPIDClusters` is used for the analysis of clusters from charged particles registered in the detector. As an analysis module, it does not actively change data in the Corryvreckan flow. Using clusters associated to tracks ensures the selection of clusters that result from real particles passing the detector. Clusters which are not associated to a track are spatially displaced from the track and are thus most likely caused by noise or particles not associated with the main charged particle source.

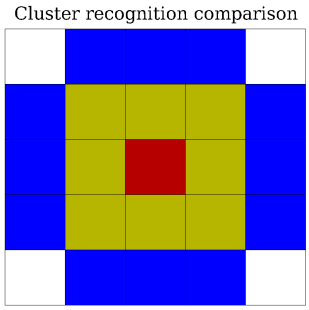

Figure 34: A pictogram visualizing the areas around a found hit (red) where `ClusteringSpatial` (yellow) and `ClusteringSpatialExtra` (yellow + blue) look for additional pixel responses to form a cluster.

In both these cases, the non-associated clusters data is not taken into account when analyzing clustering behavior of particles from the beam.
Because of the comparatively high particle rate and the trigger settings, the clusters associated to tracks are nominally the majority. Using this classification, differences between the two cases can be investigated.
In data taken from the DESY II accelerator test beam facility [57] 80 % of all clusters are associated to a track.

In figure 35 the x-axis is the average cluster size of all clusters belonging to one track. This histogram is created to combine the information from different planes for possibly finding characteristic cluster sizes which identify the projectile particle. Since only tracks are used for this plot, the contribution of noise or cosmic muons can be excluded with a large certainty. This especially is of concern, should there be tracks with a mix of different particle species in data. For the same reason, noise pixels are excluded from this figure, making the average representative for a specific energy loss. Cluster size figures from one sensor alone have a resolution of exactly one, as only whole numbers are sensible for cluster size. The resolution of figure 35 scales with the inverse of the sensor count, which is distinctively better than a single sensor.

A specific ID is assigned to any cluster referring to its shape. Figure 30 displays some shapes with their respective ID, which are consistent with their counterparts in section 4. The results of this analysis for different datasets are shown in the following.

5.3 Data analysis

In addition to which cluster sizes and shapes are present and which ones are not, recognizing any imbalance in similar cluster shapes of the same size is of interest for possible comparison with simulation results and evaluating sensor effects. Imbalances might be due to geometry effects of the pixel, or other external physical factors. In the case of ALPIDE, it is expected that clusters stretching along the y-direction are present in slightly higher numbers as compared to the x-direction. This is because of the ALPIDE pixel dimensions of 29.24 µm × 26.88 µm ($x \times y$) [39]. This asymmetry causes

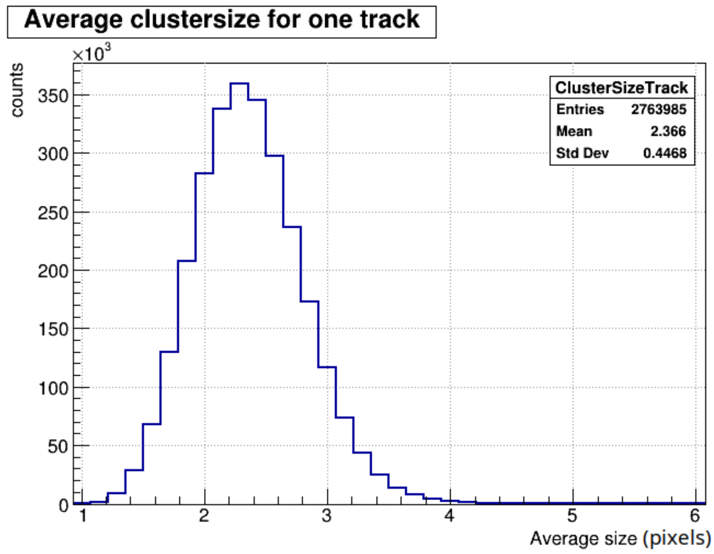

Figure 35: Average cluster size along a track plotted for all tracks. This data is from DESY electron data using a seven plane telescope, therefore seven bins in between two natural numbers are possible.

each pixel to share more charge along the shorter side to adjacent pixels, than along the longer side, since charges have a shorter distance to travel. Furthermore, the chance for a charged particle to hit in between two pixels is higher along the longer side.
These factors all contribute to clusters extending in y-direction being preferred to clusters extending in x-direction.

The settings of the threshold for all chips in this analysis have been tuned to an equivalent of 100 electrons of signal charge in the front end, which represents the nominal operational setting for ALPIDE. This value is chosen since the front end response is optimized for this case. This threshold is important since threshold is a strong contributor to cluster size.
Also, all analyzed data except cosmic muons and source data is taken at 0° incident angle.

5.3.1 One pixel clusters

The main expectation of any difference in cluster shape frequency comparing tracked clusters and clusters not associated to tracks is, that single-pixel clusters that originate from sensor noise are excluded in the first case. Since these fake hits are concerning individual detectors, tracked clusters effectively exclude any clusters stemming from non-track producing effects, such as fake hits, with a high probability.
In figure 36 two different cases are compared. In the context of this figure, tracks require a cluster on all detector planes. The two left-hand plots both only contain clusters that after completed tracking did not participate in any track. Reasons for this can be manifold. For example one sensor not detecting a particle where it passed, leading Corryvreckan to not start the

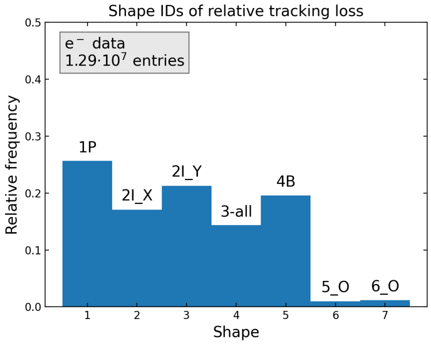

(a) Electron data, leftover unassociated clusters.

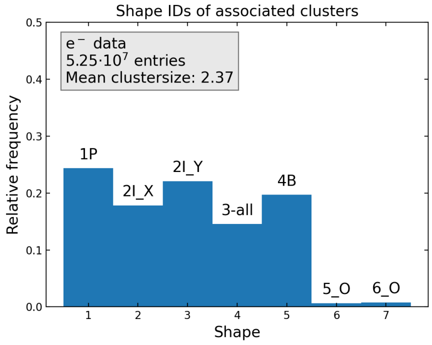

(b) Electron data, clusters associated to tracks.

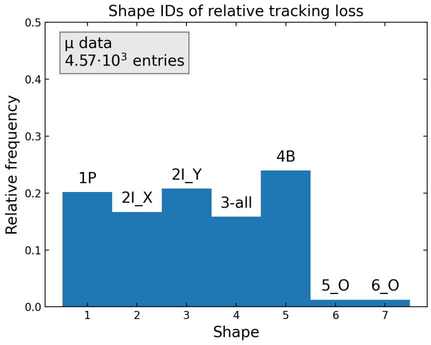

(c) Cosmic muon data, leftover unassociated clusters.

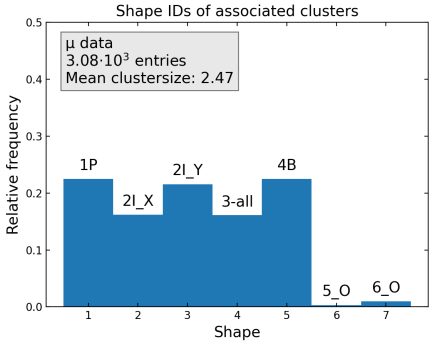

(d) Cosmic muon data, clusters associated to tracks.

Figure 36: Comparison of track clusters and leftover unassociated clusters for 5.4 GeV beam test electrons at DESY and cosmic muons. For the latter a track required to have passed through all three used detectors for a track to be formed.

tracking process in this event. Another reason could be that scattering is distorting the track such that Corryvreckan discards it due to a too large χ^2 value. A fraction of non- associated clusters are noise related and are shown as single-pixel clusters. This can be seen in the electron data subfigure 36a, where 1-pixel- clusters are represented with higher relative frequency than in subfigure 36b. The same trend cannot be confirmed for muon data, which is shown in the related figures 36c and 36d. Since the particle rate of cosmic muons is significantly lower than in a beam test, the data is less statistically significant.
The chance of randomly recording a noise hit is low, since only in the order of thousand tracks are present. In this dataset, numerous events do not have hits down to the last ALPIDE plane, as cosmic muons do not arrive at ground level within the acceptance window of the three plane telescope setup. This leads to a low yield of tracks that include a cluster from all detector planes and many clusters ending up in the histogram of unassociated clusters 36c.

For both datasets the general distribution shape for associated and unassociated clusters is similar. This suggests no large data artifacts that are excluded from tracking. However, because of sensor misalignment, clusters on the outer perimeter of the ALPIDE sensors cannot have clusters in every detector plane. Because of this, they do not participate in tracking, which causes false rejections of good clusters.

5.3.2 Two pixel clusters

The central interest in clusters of size two is the frequency imbalance of 2I-clusters in x- and y- direction. In the previous figure 36 this imbalance is already visible. In electron data, there are 24 % more two pixel clusters in y-direction than their counterparts in x-direction. This ratio varies greatly as seen in figure 36 and 40, when comparing particles with different energy losses. Americium source data with alpha particle emission as illustrated in figure 40 has as expected the highest average cluster size of all datasets and moreover features 45 % more clusters of size two in y-direction than in x-direction. COSY deuteron data displays the highest difference for this ratio, having 107 % more clusters in y-direction than in x-direction. The limited amount of muon data available displays a moderate difference, having 18 % more y-direction type clusters.
Every single value exceeds the purely geometric ratio of the ALPIDE pixel pitch of 8.7 %, because the in-pixel area responsible for creating most two-pixel clusters is delimited by other areas. In the corners of a pixel for example, four instead of two pixel clusters are created, as seen in figure 42. This effectively amplifies the geometric asymmetry effect, because the in pixel area responsible for four pixel cluster creation is not largely dependent on the pixel pitch.

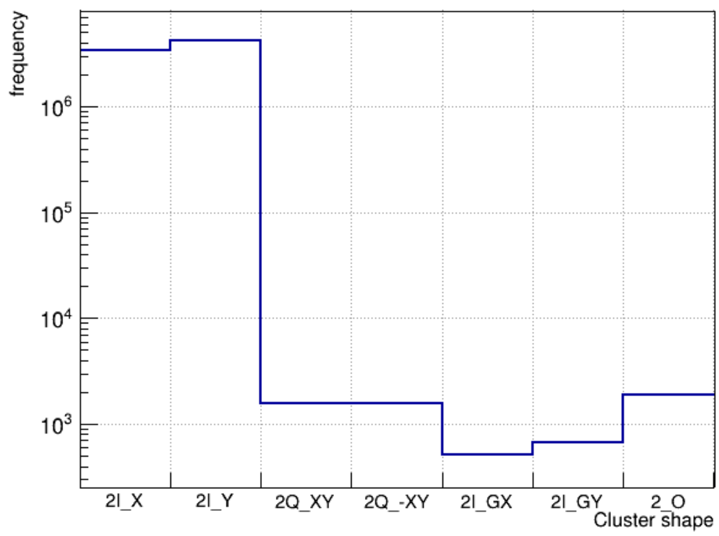

Figure 37: Frequency of two pixel clusters from electron data. As compared to the 2I-type clusters, the other shapes have a very low probability of occurring. Types 2I_G are clusters with a gap in the middle.

Additional clusters with two pixels include diagonal shapes such as the 2Q-type depicted in figure 30. To make such shapes possible, adjacent pixels must have less charge collected than their threshold, or have been inefficient. Since ALPIDE pixels are proven to be highly efficient (see chapter 3.2), both methods of how diagonal pixels are produced are expected to be suppressed. In figure 37 occurrence frequencies of all considered types of clusters involving two pixels are shown. Out of around 8×10^6 total two pixel clusters, only 0.04 % are diagonal, agreeing with the expectation of a highly efficient ALPIDE sensor, and especially the uniformity of diffusion.

Similarly to diagonal clusters, but not sharing a corner, gap clusters are also statistically suppressed. They are clusters with three pixels in a row (cluster ID 3I) with the central pixel missing, so that they only contain two hit pixels (cluster ID 2I_G). The effect of asymmetry in x-and y-directions applies here as well. The cluster shape version in y-direction has more entries than the x-direction version. Since the central pixel did not register a hit, it needs to have been inefficient, or the two single hits are unrelated. If the particle passed in the gap, but the central pixel was inefficient, some charge sharing is necessary to put the outer two pixels above threshold, but not the other two pixels adjacent to the center pixel which did not register a hit. Since the fake hit rate is low at nominal thresholds, once defective pixels are masked, the chance of making such a cluster with a gap by pure coincidence is lower than 8×10^{-9} %/event. An inefficient pixel is therefore more probable, since the inefficiency of an ALPIDE pixel at the operating point is smaller than 0.2 % [40]. In data this pixel type represents 0.015 % of all two pixel clusters. That this type of cluster is very low in frequency validates the previously mentioned expectation on frequency.

The findings for gap clusters support the standard cluster search algorithm of Corryvreckan with a trade-off. By not checking 12 additional positions, the algorithm is sped up, which is why most cluster searching algorithms implemented in Corryvreckan, focus on touching neighbor search.
Additionally, for cases of high particle rate it might be wrong to classify hits further apart as one cluster, since they might as well exist because of two independent particle hits.
Finally, around ≈ 0.01 % of two pixel clusters are left over unidentified and thus are classified with the shape ID 2O as the 'others' group. This group contains all clusters of size two that do not have a shape covered by the other IDs. These would contain clusters with hits spaced by a gap diagonally, which are not relevant on the basis what was discussed so far.

5.3.3 Three pixel clusters

99.5 % of size three clusters are 'L'-shaped. There are four L-shaped clusters of size three (see figure 30), which are expected to have the same frequency. This is because the pixel pitch asymmetry does not cause any particular version of this shape to be statistically preferred. From the middle point of the 2x2-pixel square that forms the 3L-cluster every shape has both a long and a short edge inside the cluster. This means that there is no imbalance in charge sharing stemming from geometrical cluster properties.

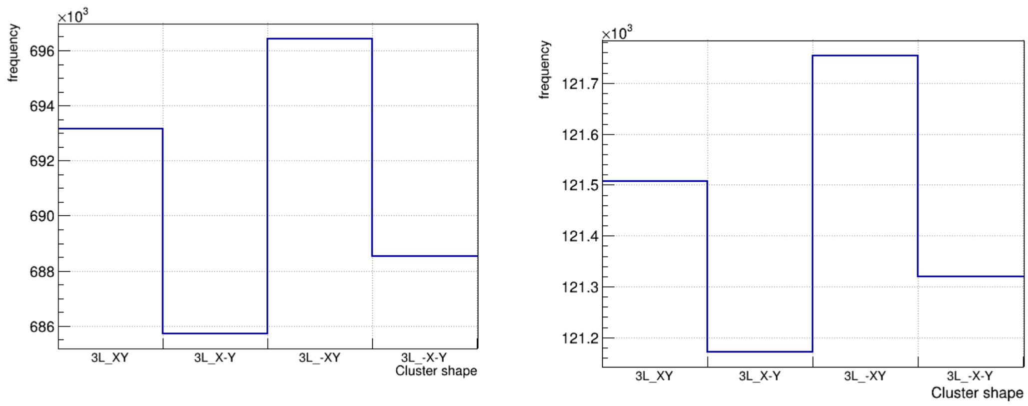

(a) Electron data using tracked clusters.

(b) Deuteron data using all clusters.

Figure 38: Cluster shape frequencies histogram for 3L-clusters using DESY electrons and COSY deuterons.

This hypothesis is supported by data. As seen in figure 38, the imbalance between the individual shapes is around 1.43 % in the case of electrons. For deuterons the imbalance is about 0.49 %. This is less, but still above any expected level of counting uncertainty, which is given by the inverse of the square root of the counted cluster numbers [58]. With counts as high as 7×10^5 for electrons and 1.2×10^5 for deuterons, the worst-case statistical uncertainty for both cases is 0.12 % and 0.29 %, respectively. While this is not an overly pronounced imbalance, a very similar pattern is found throughout all datasets. This applies especially to both beam test data used for analysis here, as visible in figure 38.

Additional clusters of size three include low counts ($\approx$ 1.7 % of three pixel clusters in electron data) of elongated clusters (shape ID 3I). In this case clusters in x-direction having about double the frequency of those in y-direction, with the same reasons that applies to the respective 2I variants. All other shapes include parts that are diagonally arranged or have gaps and thus are present in negligible counts.

5.3.4 Four pixel clusters

98.6 % of all four pixel clusters are of shape 2x2 pixels (shape ID 4B). Figure 39 gives an overview on the counting rate of different four pixel cluster shapes. Long clusters (shape ID 4I) now become very unlikely to be formed, given that diffusion is isotropic and therefore the shape id 4B is heavily favored, with the 4T cluster second most probable. This is reflected by the data, as it can be seen that long clusters are only present in very low counts. Both types accounting for about 0.02 % of four pixel clusters.

Out of the two possible directions of the 4I cluster elongation, the one in y-direction has 133 % more entries than the one in the x-direction. The reason

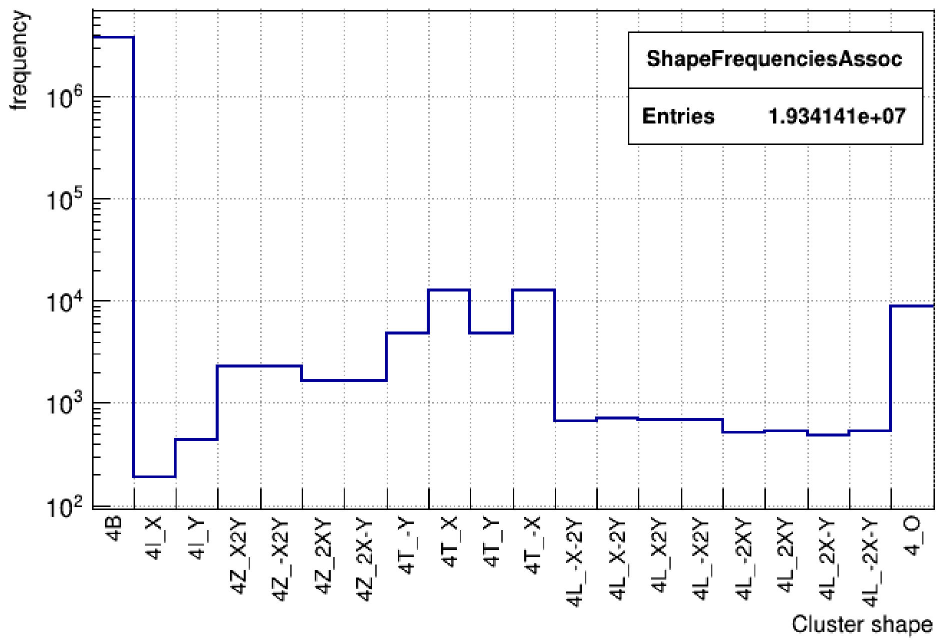

Figure 39: Cluster shape frequency of associated four pixel clusters observed in electron beam test data from DESY.

is exactly the same as for the 2I cluster pair. The ratio of relative frequency for the elongated cluster pair gets higher with increasing size. Additionally, the total numbers of these clusters go down as size increases. This is because that longer clusters, that do not increase in width as the total size increases, need increasing amounts of pixels that do not receive charge above threshold. This is improbable given the isotropic nature of charge diffusion.

Other shapes include the 4Z shape. It is a 2x2-px-cluster with one row shifted by one pixel to form a Z shape. This shape has four different versions, which are obtained by rotating and mirroring the shape. In total, roughly 0.18 % of all four pixel clusters belong to the 4Z shape. 58 % of those are of the two versions three pixel rows high, as seen in figure 39.

The next shape in consideration is the 4T-shape with its four different configurations in the two axis directions. These clusters are a 3I shape with one additional hit pixel adjacent to the center pixel, thus forming a T. This cluster has the second-highest frequency after the 4B shape. It occupies 0.9 % of all size four clusters. Here, the versions three rows high have vastly more counts, with an imbalance of 160 % more counts than their counterparts. This is because the Y version has the 3I part of the shape oriented in the x-axis direction. As compared to the 3I clusters, which have fewer counts than their 4T counterparts, adding a cluster to the center pixel of the row the cluster gets wider. This makes it more likely to appear in data since it is now more compact. More compact cluster shapes are more likely to appear since they fit well with the isotropic diffusion.

5.3.5 Five and more pixel clusters

In minimum ionizing particle beam test data the main present cluster shapes are the ones thus far discussed, and any clusters with higher pixel counts are only present in relatively low counts. This is because the amount of charge liberated through ionization from a minimum ionizing particle is in the majority of cases not enough to bring pixels distanced more than one pixel pitch from the incidence point above threshold. This is due to the solid angle getting small, the diffusion length being more of a factor in limiting charge counts, and the depletion region of other pixels keeping charges from diffusing further.
The DESY electrons practically behave like minimum ionizing particles. Thus, mostly smaller clusters are produced. From the data it can be calculated that only about 1 % of all clusters have a size above four pixels. In contrast to that, source data has low momentum decay products with significantly higher energy loss per micrometer travelling distance in silicon than minimum ionizing particles.
Alpha particles from ^{241}Americium decay have 5.5 MeV of kinetic energy, resulting in a very high energy loss and a range of only 43 µm in silicon. This means that within the travel path of an alpha particle, all on average $\approx$ 5.5 MeV of kinetic energy are deposited into the silicon. Therefore, they produce larger clusters.

An experimental setup has been built using two planes of ALPIDE sensors with a distance of 2 cm apart. The source ^{241}Am for taking data was placed only few mm above the first sensor (ALPIDE 0), in order to minimize the energy lost by ^{241}Am alpha decay particles in air. This energy is significant, since alpha particles from a ^{241}Am source have a range of only a few centimeters in air.
Data has been taken in two different configurations, exposing both sides of the sensor to the source. First when placing the source above the sensor, radiation first penetrates through the circuitry layer, then through the deep p-wells until finally reaching the sensitive epitaxial layer 10 µm below the chip surface. Secondly, when illuminating the sensor from below, the radiation passes through the substrate and then reaches the epitaxial layer of ALPIDE 1 first.
Figure 40 shows cluster size frequencies from both versions of the ^{241}Americium experiment setup. The first sensor exposed to the source from above is the only dataset that showed a significant amount of clusters beyond a size of 6. Figures 40a and 40b show cluster shape distributions for alpha particles shot on the ALPIDE sensor surface, while figures 40c and 40d show the case when the source is placed in front of the ALPIDE 1 substrate.
Figure 40 displays three similar cluster size distributions. The one exception being the one from the chip, which was closest to the source in the frontal configuration, ALPIDE 0. One possible explanation for the high average cluster size of 4.9 pixels with respect to electrons from the beam test is the detection of clusters which result from large energy deposits by the incident alpha particles. ALPIDE is only 50 µm thin [40], which captures them fully.

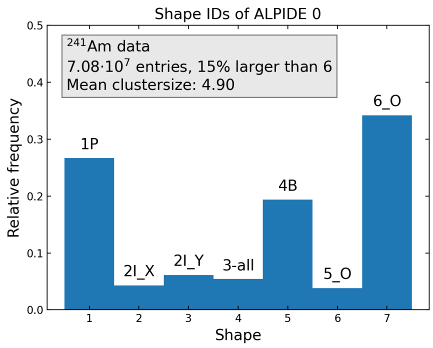

(a) Cluster size on the first sensor.

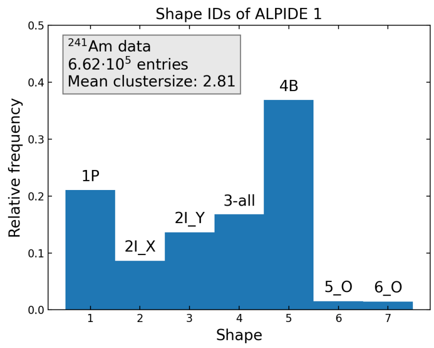

(b) Cluster size on the second sensor.

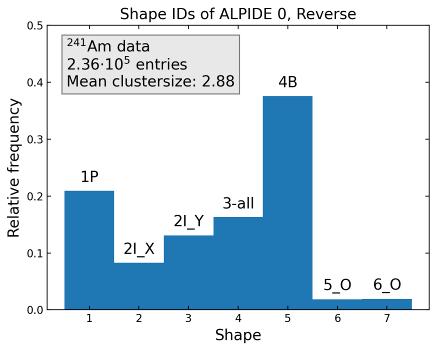

(c) Cluster size on the first sensor. Particles coming from the back side.

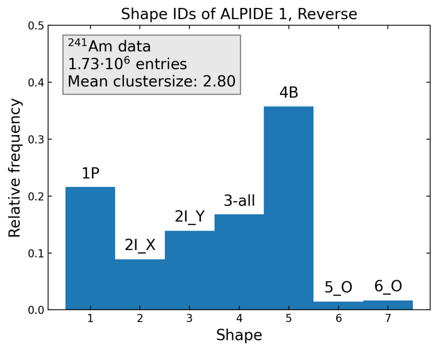

(d) Cluster size on the second sensor. Particles coming from the back side.

Figure 40: Cluster shape frequencies from measurements with ^{241}Am as alpha source. The averages are including all clusters, not just the ones shown here. For back side illumination, sensor ALPIDE 1 is the first one in the particle path of travel.

In the sensor about half of this energy is deposited in the substrate material at the bottom of the sensor and in the circuitry, where the contribution to the signal charge can be neglected.
Source generated alpha particles have very limited range in materials, which can be verified by looking at the total hit counts on the second ALPIDE sensor placed 2 cm behind the first one, which are on the order of 100 times lower.
The considered alpha particles with the energy in question have a range of 43 µm in silicon and 4.18 cm in dry air [56]. The total amount of material until the second sensor's epitaxial layer is first 1.188 µm of gold film together with 1.812 µm of palladium as protection on the source itself [59]. Then 2 mm of air from the source to the first sensor, then approximately 50 µm of silicon, then 2 cm of air and finally ≈10 µm of silicon until reaching the sensitive volume in the second sensor. When illuminating the ALPIDE sensor from the back side, the air distance to the substrate layer was kept at 2 mm as well, to keep results as comparable as possible.
Calculating the range with the expected average stopping power, the alpha

particles leave the source with approximately 4.25 MeV energy left. Traversing the layer of air, they have a final energy upon hitting the ALPIDE surface of 4.04 MeV. The range of alpha particles in silicon with this energy is 24 µm, enough to hit the epitaxial layer [56]. This range is however not enough to penetrate a whole ALPIDE chip by a factor of two, and therefore get absorbed in the first sensor. Clusters from particles having traversed the setup under a higher incidence angle α will especially be absorbed, since the travelled distance increases with the inverse cosine $1/\cos(\alpha)$. This dictates the absence of alpha particles in the second ALPIDE sensor, and points to other decay products being recorded in the second detector.

The mechanics explained above lead to few particles reaching epitaxial layers in all geometrical configurations of the experimental setup, except ALPIDE 0 being shot at from the top, which has the epitaxial layer directly below a 10 µm layer of circuits for the pixel electronics [40]. And since these alpha particles don't reach far, this results in the distributions with the highest cluster sizes when the epitaxial layer is closest to the source.

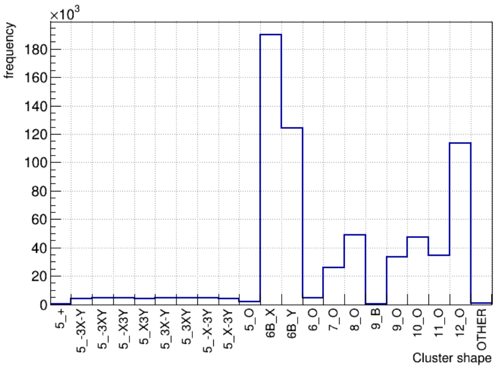

(a) Clusters with sizes of five and more from ^{241}Americium source data. Measured with a single sensor illuminated from the front. The histogram displays 51.9 % of all data.

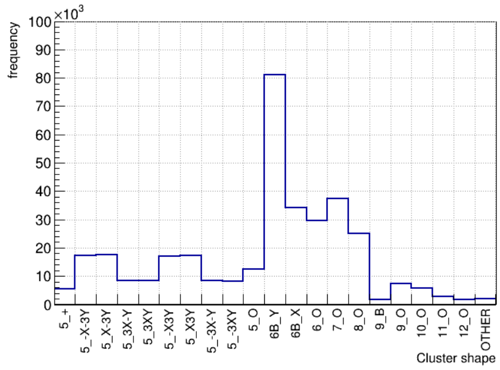

(b) Clusters with sizes of five and more from electron beam test data. This histogram displays 1.8 % of all data.

Figure 41: Cluster shape frequencies for clusters of size five and larger from measurements with an alpha source and electron beam test data. The OTHER class represents clusters of size 13 and larger, which are not considered otherwise.

The cluster frequency data from this sensor (ALPIDE 0) is visualized in histogram 41a.

For alpha particles, the one-pixel cluster frequency is unexpectedly large. This could be the result of 59.5 keV gamma particle emitted from ^{241}Am. That 50.65 keV gamma particles can result in a signal if ALPIDE was shown by [17], but the attenuation is very low at this energy range, not being able to fully explain this large peak of one pixel clusters. However, gamma particles will penetrate the first layer of ALPIDE, and continue on to the second layer to create a signal there aswell, explaining the 100-times lower hit count in ALPIDE sensors not exposed to the primary alpha radiation.

Most five pixel clusters in figure 41a are of 4B-type with an extra pixel added on the outside. This shape has eight versions and makes up 94.2 % of all size five clusters. Electron data is confirming this observation. Here, 90 % of all 5-clusters are of this shape.
Furthermore, electron data displays double the amount for five-clusters that extend further in x-axis direction as compared to source data. This difference might be caused by the difference of energy deposited in the epitaxial layer. Electrons from the DESY accelerator are minimum ionizing particles, creating a median 60 electron-hole pairs per µm as per the Bichsel energy loss equation [15]. Alpha particles from ^{241}Americium have significantly higher ionization potential, creating $\approx 44\,300$ electron-hole pairs per µm on average [56].
Therefore, minimum ionizing particles create five pixel clusters from less charge than the alpha particles, favoring cluster shapes that possibly need less charge to be formed.

Clusters of size six are split mostly between the two 2x3 block versions. For electrons 20 % of all clusters of size six belong to shapes that differ from these two block forms. The shape in y-direction has significantly more counts relative to the shape elongated along the x-direction, with 56 % of all size six clusters in the electron dataset belonging to the version three rows high (shape ID 6B_Y).

For higher cluster sizes only very limited information can be taken from figure 41. For clusters of size nine the majority are not represented with a 3x3 hit pixel grid (shape ID 9B). This might be explained by the rectangle pixel shape, leading to other cluster shapes being preferred. The nature of these shapes can be subject of further studies in this direction.

5.3.6 In-pixel cluster shape studies

Using the DESY electron data in order to profit from good sub-pixel spatial tracking resolution, the most frequent cluster shape as a function of on the track in-pixel position is plotted in one representative pixel in figure 42. Since only most frequent clusters are used to color the bins, the borders between the individual areas seem sharply defined because the underlying shape distribution per sub-pixel position is ignored. This makes it possible to identify ares predominantly responsible for formation of certain cluster shapes.

The plot displays a clear correlation of small cluster sizes with particle hits close to the pixel center, where the central pixel diode is expected to have its greatest effect in preventing charges to diffuse to other pixels, potentially resulting in a larger cluster size.
Two pixel clusters are mainly produced with hits close to the center of two pixel edges, where most charges would be caught by both adjacent pixels.

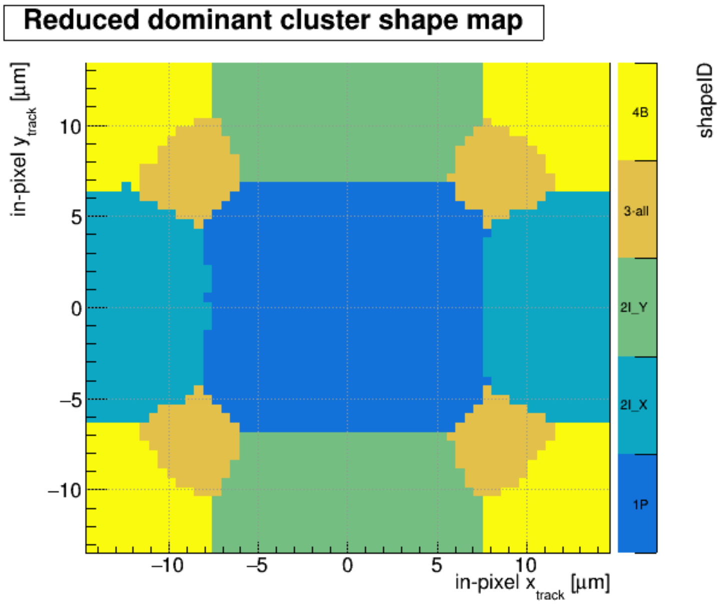

Figure 42: Dominant cluster shape as a function of the associated track intercept position on the sensor, using DESY electron data.

Here the asymmetry of pixel pitch comes into play as the relevant sensitive area for the formation of two pixel clusters strongly depends on the geometry. Four pixel clusters are mainly produced for particle hits in the corner of pixels, and subsequently all charges from it will distribute themselves among the four neighboring pixels.
The area most important for three pixel hits is recorded between the area for one and four-pixel clusters. Charges diffusing from here are reasonably close to two of the three adjacent pixels, having a higher diagonal distance towards the pixel that is missing to a 2x2 pixel cluster.
The total area of the individual domains for different cluster shapes can be interpreted as a measure for shape frequency, since incident particles hit inside one pixel equally distributed.
The above observations are qualitatively consistent with the simulation result, shown in figure 29.

6 Discussion and Outlook

6.1 Comparison between simulation and data

The performance of the computational model explained in section 4 can be assessed through comparing its cluster size and shape predictions to analyzed beam test data. Since in simulation the passing particle is assumed to be minimum-ionizing, the experimental data set needs to be chosen accordingly. Because of the factors explained above in the subsections regarding the cosmic muon data 6.3 and data of decay products from a radioactive source 6.4, the simulation output is compared with the minimum-ionizing electrons from the DESY beam test.

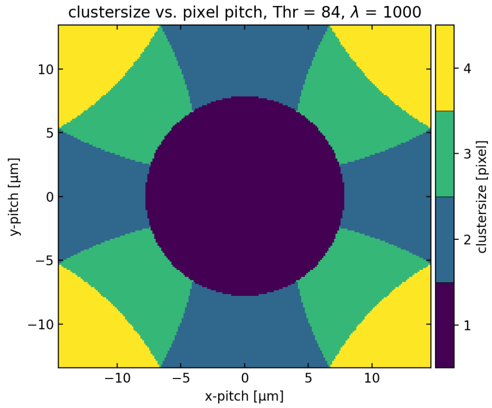

(a) Simulation cluster shape per in-pixel position of simulated particle incidence. Best-fitting simulation result for the center radius = 7.8 µm

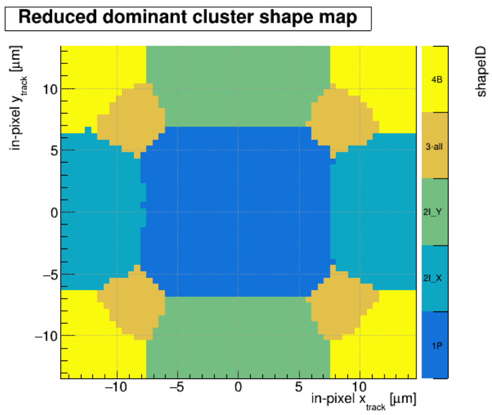

(b) Electron dominant cluster shape per in-pixel position of traversing charged particle path.

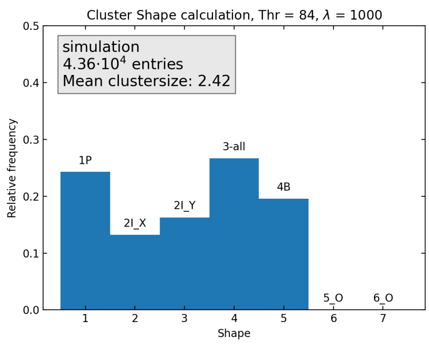

(c) Simulation cluster shape frequencies.

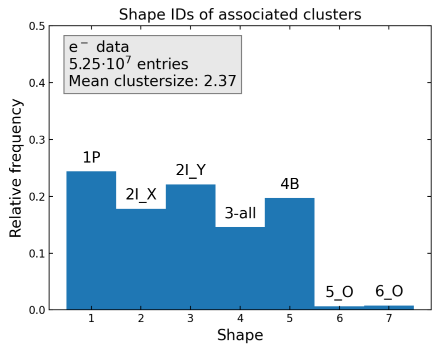

(d) Electron relative cluster shape frequencies.

Figure 43: Comparison of cluster shape results from simulation and electron beam test data.

Figure 43 shows cluster size frequencies and dominant cluster shape 2D histograms depending on the impinging point of a traversing charged particle for simulation and data. The simulation predictions are on the left two plots, with the electron data to the right. Several differences can be identified using these plots, however the simulation has two important tuneable features that significantly impact results.

The first one is the central drift radius. As explained in section 4, it is a simple implementation of a drift area which prevents charge from diffusing to other pixels. The radius has been fitted to match the one pixel cluster relative frequency observed in data. The value for the radius fits well with the physical assumptions one can make about the ALPIDE depletion region, underlining the accuracy of the model. This radius changes with the applied bias voltage, and therefore the model can also account for drift and reverse bias.

Secondly, the discriminator threshold for the pixels can be changed to adjust the charge adjacent pixels need to carry in order to register a hit. For all data types that are analyzed, the threshold is tuned to 100 electrons. This can not be tuned with arbitrary precision, but the threshold mean over the entire ALPIDE chip is within 3 % of 100 electrons, as seen in figure 20. Due to the complex circuitry on the ALPIDE sensor, recreating the exact threshold in simulation is rather hard. The simulation has its threshold adjusted to 84 electrons, to match the relative frequency of clusters of size four. This increase in threshold can also be physically motivated. The implementation of drift in the computational model is comparatively simple, and thus has some definite shortcomings. As such, a particle passing at the edge of the depletion region relatively far from the pixel center in reality would still deposit a large portion of its energy into a volume of the epitaxial layer which does not have strong electric fields for drift. This would effectively lead to a contribution to neighboring pixel signals, and possibly cause them to collect enough charge for a hit to be registered. In the simulation model, this contribution is simply ignored. All charge carriers that come from a particle passing closer than a specific radius from the pixel center are immediately collected. This results in cumulatively less charge diffusing than it would be the case otherwise. To counteract the threshold can be tuned lower to make the measurement more sensitive. Due to the simplicity of the depletion implementation, the area of particle impinging points resulting in one pixel clusters is circular, while the same region in data looks more similar to a square with cut off corners. The general location of in-pixel regions where clusters of size two, three and four are predominantly produced are agreeing between simulation and data analysis. However, their shape is not simulated entirely correct. This might be a problem of the data analysis method, as for each sub-pixel track position the most probable cluster size is registered, discarding any information about the shape ID distribution within. Or it might simply be a deficit of the simple diffusion model that forms the basis for figure 43a.
While the asymmetry between the two cluster types of size two match within reasonable deviation, the relative frequency of three pixel clusters is not correctly reproduced in simulation. This is a systematical error inherent to this simulation, which overestimates three pixel clusters. This might hint to

some other charge sharing effects rather than diffusion only, such as capacitive coupling between the individual adjacent pixels playing a role, which have not been included in the simulation so far. If this effect is considered, the induced signal of two adjacent pixels above threshold might be able to influence a pixel strongly enough that instead of a 3L type cluster, a 4B type is produced. This would increase four pixel clusters relative to three pixel clusters. However, for how simple the simulated model for charge diffusion and drift is, the results do in large parts match the respective data it was intended to describe.

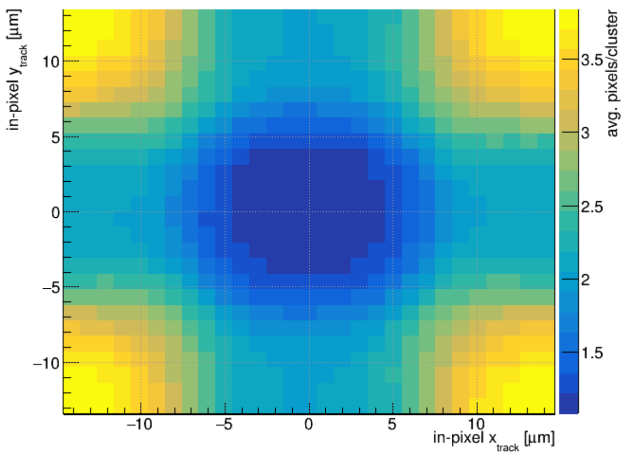

Figure 44: In-pixel average cluster size dependence of the associated particle hit position from DESY electron data.

Figure 44 is an alternative to figure 43b, where not the most probable cluster size is considered, but the average cluster size relative to the associated track position is computed. Given enough tracks as in this case, a smooth gradient can be observed, while a distinct circular shape in the center makes the influence of the collection diode very obvious, just like the circular area introduced in the simulation. It is also noted that the overall average cluster size simulated differs only by 0.05 pixels from data. The simulation predicts significantly more three pixel clusters than data. On the contrary, clusters larger than five pixels in data are present in low counts, but they are not produced in the simulation. This influences the average cluster size, equalizing it. This plot does not clearly mark the area where three pixel clusters are produced, as there is no specific region where a track intersection would result in three pixel clusters, but actually a continuum of places between one, two and four pixel clusters. Since the amount of charge freed is a statistical process, the average size is more representative of this distribution. Moreover, the individual areas giving rise to different cluster sizes in figure 44 are generally more spherical than the respective areas in figure 43b. This is due to the formation of averages with an in-pixel uncertainty of the tracking error, which is not present in simulation.

6.2 The role of the ALPIDE sensor substrate in simulation

As seen in previous sections, the simulation describes the data qualitatively, but not without error. The simulation also discarded some known sensor aspects in order to simplify the model, and speed up calculation. To evaluate the necessity to include all contributions and roles of the ALPIDE substrate on the simulation result, it is useful to discuss the influence of this layer more closely, and especially to quantify this influence.

The substrate of ALPIDE sensors is heavily doped with an acceptor density of approximately $n_a = 10^{18}\,\mathrm{cm}^{-3}$ [45]. This heavy acceptor doping concentration results in a 25 µm thick layer with a resistivity of 20 mΩ cm to 70 mΩ cm (see equation 6, with doping in [45]). Therefore, the lifetime of electrons excited to the conduction band is greatly reduced compared to the epitaxial layer, and thus the diffusion length is also reduced. In this case, the corresponding diffusion length is between approximately 10 µm to 100 µm. This is of the order of the substrate itself, which allows some electrons to reach the border of the epitaxial layer. This also means that inaccuracies in doping concentration have a larger impact on electron - hole recombination than in the epitaxial layer.

The substrate does not feature any significant electrical fields owing to the absence of any n-type dopants in the region, and that the depletion voltage is not sufficient to extend the depletion zone into the highly doped substrate. Unlike the epitaxial layer, there are no drift regions and charge carrier movement is described by diffusive propagation alone. Assuming that charge carriers can also cross from substrate to the epitaxial layer with no significant losses, they can lead to a contribution to total charge collected at the detection diode. According to the computational model presented in section 4, the closest pixel could register a signal increase of 12 % to 18 % relative to the previous signal when ignoring the substrate contribution. These values were calculated using the integrand from equation 20 presented in section 4, modified for diffusion from further distances, ignoring the larger diffusion length for the epitaxial layer.

Since the substrate is further away from the pixel surface where charges are collected in the simulation, charges from the substrate are spreading across the pixels above more evenly which causes a larger signal contribution. In the case of an example pixel one pitch in x and y- direction away from where the simulated particle path is, the collected electron count is increased by 10 % to 30 % with respect to ignoring ionization in the substrate, depending on the chosen value of the doping concentration in the substrate. Due to the steep increase in complexity the signal contribution from substrate electrons is neglected in section 4, which might be a subject of future improvements.

Another effect of the substrate is its role in reflecting electrons that diffuse in the epitaxial layer away from the detection surface. The difference in doping concentration of five orders of magnitude between the ALPIDE epitaxial and substrate layers leads to the formation of a potential barrier, which causes electrons in the epitaxial layer to be reflected away from the substrate boundary layer, back into the epitaxial layer [43]. While this boundary layer is not generally proven to be perfectly flat, semiconductor boundary layers can be produced to a very high precision according to their specifications. For the purposes of the presented simulation, assuming a perfect reflection, where the incidence angle is equal to reflection angle is sufficient to qualitatively investigate clusters on ALPIDE sensors. Any perfect reflection can be constructed as if the reflected beam originates from behind the reflection plane. Utilizing this methodology, the particle path is simply extended by the length of one epitaxial layer depth further. Then it is integrated along the entire path (50 µm), with all particles diffusing upwards to the sensor surface.

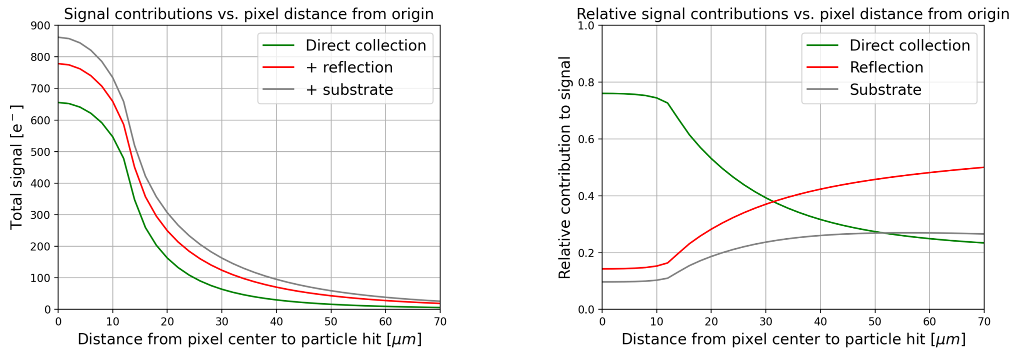

(a) Cumulative signal contributions.

(b) Relative signal contributions.

Figure 45: Signal contribution visualization from direct collection, reflection at the substrate barrier and from the substrate itself. Distance is measured along the x-axis, i.e. larger ALPIDE pixel pitch.

In figure 45, the individual contributions from the epitaxial layer directly, reflection on the substrate and substrate ionization to the total charge collected in a pixel is visualized considering these contributions isolated from one another. The distance shown on the x-axis is measured from the particle hit point on the detector surface to the center of the pixel picking up the signal plotted. In these plots, only diffusion is considered. The values for signal contribution from electrons coming from inside the substrate (gray) have been estimated using the most adequate value for the diffusion length range in the substrate, 30 µm. Additionally, the substrate contribution uses a simpler implementation of diffusion recombination, in order to implement it into the same model. The error of this implementation is estimated to be lower than 2 % of the total signal. To assess the reflection contribution, the calculation is carried out by only integrating over the reflected, i.e. virtual part of the epitaxial layer. The contribution of electrons reflected by the substrate to a signal induced into a pixel closest to the particle path is 25 %. Similar to the contribution from the substrate the reflected relative signal contribution rises with larger distance of simulated particle path to considered pixel center. At a distance of half a pixel pitch from the particle incident point, the total signal drops off significantly. This is due to the particle trajectory point of incidence leaving the area directly below the pixel under investigation, which greatly reduces the space angle that diffusion paths can have to still reach the pixel. As a result, the total amount of charge collected is reduced greatly. Because the direct contribution originates from an area closest to the detection surface, it is affected the most, as visible in figure 45b, where the contributions relative to the total signal are plotted.

The large contribution of reflected electrons emphasizes the importance of considering reflection at the substrate boundary layer for cluster size evaluation, since without this consideration significantly less charge would be shared across pixels. The high contribution from the substrate points to the possibility to include this aspect in future studies, necessitating a more complicated implementation of diffusion length in the theoretical model. Additionally, the epitaxial layer is not fully depleted and charge carriers that reflect off the substrate spend more time diffusing before entering the influence of the electric fields, which are present in the upper part of the epitaxial layer. This makes such an improved model more accurate to describe the spreading of charges, since drift is not considered.

6.3 Cosmic muon data

Cosmic muons as well as electrons from the DESY beam test campaign fulfill the criteria of being minimum-ionizing-like particles. However, cosmic muon data is only available in very limited quantities, because the production of cosmic muons is a natural process providing particles within the acceptance of the sensor telescope in a low rate [60]. Figure 36 shows electron and muon data having little discrepancies in relative cluster size distribution. The statistical significance of muon data is not ensured, as a total data size of $\approx$600 tracks in each of the five major cluster size intervals leads to significant statistical counting error of $1/\sqrt{600} = 4\,\%$ in sampling the underlying distribution. For this reason, only electron data is used for the comparison with the theoretical model.

6.4 Americium decay data

Alpha particles from Americium decays have been used to increase the signal created in the epitaxial layer by increasing the energy loss in the sensitive volume. This enables the study of large clusters in ALPIDE sensors, that are normally produced in very low counts using minimum-ionizing particles. However, because of their limited range in silicon and air, these alpha particles are not suitable for reconstructing particle tracks as they cannot cross several detectors. For in-pixel statistics multiple crossed detectors and a well performing tracking algorithm to determine the track point of incidence to sub-pixel precision would be needed.

Additionally, an unexpectedly high rate of one pixel clusters is observed in the Americium data with a fraction of 9.7 %. This is unexpected because

of the large energy loss of alpha particles in the epitaxial layer. Especially outside the depletion region with its extents as calculated in chapter 4, there should be enough charge carriers to diffuse and bring neighboring pixels above threshold. Since this is not the case, there must be either issues with assumptions about the depletion region, which is not very likely, or there is a process that creates one pixel clusters in significant numbers.
One possibility is the decay scheme of ^{241}Am, which contains gamma particles as decay products. The cross-section for photons interacting with silicon

Energy (keV)	Emission (%)	Attenuation (%)
59.54	35.9	0.19
26.34	2.4	1.20
33.20	0.1	0.65

Table 2: Major ^{241}Am non-alpha emissions with emission and attenuation probability [55] [61].

differs heavily from that of charged particles. In general, photons can create a signal in the ALPIDE epitaxial layer primarily through the photoelectric effect. At the relevant photon energies shown in table 2, silicon becomes very transparent to X-rays, and thus no large signal can be expected to explain the observed amount of single pixel clusters.
Another possible source for one pixel clusters is a possibly not perfectly light-shielded experimental setup. At data taking time, the entire setup including the Americium source was placed under a cardboard box. Since the setup needed to be connected for data taking and power distribution purposes, small openings in the light cover could not be avoided. If enough photons hit a pixel to bring it over threshold, this would result in an amount of one pixel clusters. This would be visible on both sensors since they are sufficiently spaced for scattered light to hit both sensors. But as visible in figure 40, the single pixel clusters are present in ALPIDE 1 in greatly reduced numbers just like the other cluster shapes.
Another possible theory concerns the reach of alpha particles in the epitaxial layer. As calculated in section 5.3.5, the alpha decay particles have a very limited reach in the sensors. This might lead to some particles getting absorbed while traversing the epitaxial layer. If they hit very central on one pixel, inside the depletion region of the collection diode, they might be absorbed while still inside the depletion region, thus not contributing any liberated charge carriers to diffusion, since all are collected by the central collection diode. But this theory cannot be decisively proven without good in-pixel hit resolution.
As a conclusion, the large amounts of size one clusters remain largely unexplained. This issue needs to be subject of further investigations. Possibly a second measurement, addressing a perfect light shielding to rule light out as source of the one pixel clusters would be advised.

6.5 Summary and conclusion

A basic model for charge diffusion and drift within a silicon pixel sensor has been developed in order to investigate clustering behavior, with focus on cluster size and shape. Its parameters have been tuned to data analyzed from real sensors. Results indicate that the model seems to simulate cluster shapes in ALPIDE sensors in a qualitative way. The same trends can be observed, which is remarkable given the simple assumptions that build the base of the simulation. The theoretical model has a few inaccuracies, for example the overestimating of size three clusters or the exact in-pixel shapes that produce them. Nevertheless, the overall behavior of charge sharing via diffusion has been successfully implemented in a model that produces cluster shape distributions similar to the ones found in the ALPIDE sensor. Implementing more complicated models for substrate, drift and the depletion zone are promising fields of study for possible future expansions of this theoretical model.

A Cosmic muon data rate

The data used in figure 36 for cosmic muons has been gathered over the course of two days, and contain a total of 1031 valid three-plane tracks. The electron data in the same figure is comprised out of a total of around 10^7 events, which at usual test beam rates can be taken in a few hours. Assuming a day for the electron data, the time it would take to get the same track number out of cosmic muons can be straightforwardly extrapolated as

$$t = 2d/1031 \cdot 7.5 \times 10^6 = 39.86a. \tag{26}$$

This emphasizes the need for beam test campaigns, as normal detector development needs to advance during significant shorter timespans.

B All cluster shape identities

Below in figure 46 are all cluster shape IDs that exist in code, of which not all are important or discussed in this thesis.

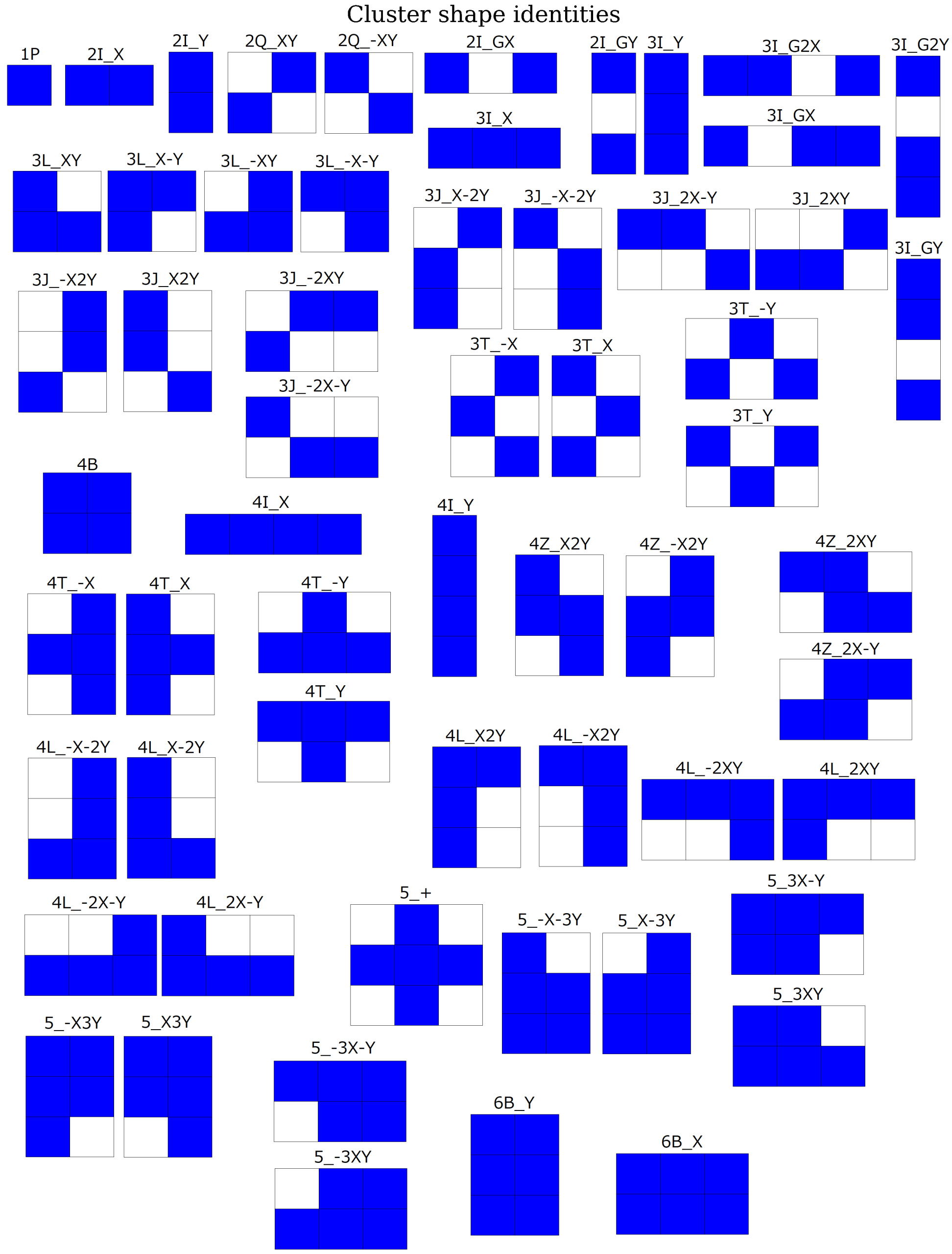

Figure 46: All cluster shape IDs

References

[1] *CERN Our People*. URL: https://home.cern/about/who-we-are/our-people (visited on 01/05/2023) (cited on page 1).

[2] *CERN Experiments*. URL: https://home.cern/science/experiments (visited on 01/04/2021) (cited on pages 1, 2).

[3] *The CERN site*. URL: https://cds.cern.ch/record/2693837/files/Poster-2019-858.pdf (visited on 01/04/2023) (cited on page 1).

[4] *Large Hadron Collider beauty main page*. URL: http://lhcb.web.cern.ch/ (visited on 01/20/2023) (cited on page 2).

[5] Werner Herr and Bruno Muratori. "Concept of luminosity". In: (). URL: https://cds.cern.ch/record/941318/files/p361.pdf (cited on page 2).

[6] *HL-LHC operational scenarios for Pb-Pb and p-Pb operation*. URL: https://cds.cern.ch/record/2722753 (visited on 01/08/2023) (cited on page 2).

[7] Giacomo Contin on behalf of the ALICE Collaboration. "The MAPS-based ITS Upgrade for ALICE". In: (2019). URL: https://pos.sissa.it/373/003/pdf (cited on pages 2, 4, 5).

[8] *Latest results on the production of hadronic resonances with ALICE at the LHC*. URL: https://indico.mitp.uni-mainz.de/event/191/contributions/3153/attachments/2446/2635/20200122Agrawal_Bormio.pdf (visited on 01/07/2023) (cited on page 2).

[9] *A Large Ion Collider Experiment*. URL: https://alice.cern/ (visited on 01/04/2023) (cited on page 2).

[10] *ALICE Schematics*. URL: https://cds.cern.ch/record/2263642 (visited on 01/05/2023) (cited on page 3).

[11] C. Fabjan and J. Schukraft. "The story of ALICE: Building the dedicated heavy ion detector at LHC". In: (2011). DOI: 10.48550/ARXIV.1101.1257. URL: https://arxiv.org/abs/1101.1257 (visited on 01/10/2023) (cited on page 2).

[12] *The ALICE Detectors*. URL: https://alice.cern/alice-detectors (visited on 01/05/2023) (cited on pages 3, 4).

[13] The ALICE Collaboration. "Technical Design Report for the Upgrade of the ALICE Inner Tracking System". In: (Nov. 7, 2013). URL: https://cds.cern.ch/record/1625842 (cited on pages 3, 5, 22, 26).

[14] Stephane et.al. Fartoukh. "LHC Configuration and Operational Scenario for Run 3". In: (2021). DOI: https://cds.cern.ch/record/2790409 (cited on page 4).

[15] P.A. Zyla et al. (Particle Data Group). "Passage of Particles Through matter". In: (2020). URL: `https://pdg.lbl.gov/2020/reviews/rpp2020-rev-passage-particles-matter.pdf` (cited on pages 5, 9–12, 28, 29, 42, 54).

[16] Valentina Raskina and Filip Krizek. "Characterization of Highly Irradiated ALPIDE Silicon Sensors". In: (2019), pp. 2, 3. URL: `https://bora.uib.no/bora-xmlui/bitstream/handle/1956/18057/Masters-Thesis_Dept-of-Physics_Susmita-Afroz_June-2018.pdf` (cited on page 5).

[17] Susmita Afroz. "Noise and Cluster Size Studies of ALPIDE-CMOS Pixel Sensor for pCT". In: (2018). URL: `https://bora.uib.no/bora-xmlui/bitstream/handle/1956/18057/Masters-Thesis_Dept-of-Physics_Susmita-Afroz_June-2018.pdf?sequence=1` (cited on pages 5, 53).

[18] *Longer term LHC Schedule.* URL: `https://lhc-commissioning.web.cern.ch/schedule/LHC-long-term.htm` (visited on 01/30/2023) (cited on page 5).

[19] Magnus Mager. "Upgrade of the ALICE ITS in LS3". In: (2019). URL: `https://cds.cern.ch/record/2747243` (cited on page 5).

[20] Wikimedia Commons. *File:Standard Model of Elementary Particles dark.svg — Wikimedia Commons, the free media repository.* [Online; accessed 08-March-2023]. 2020. URL: `https://commons.wikimedia.org/w/index.php?title=File:Standard_Model_of_Elementary_Particles_dark.svg&oldid=510617339` (cited on page 6).

[21] M. Thomson. *Modern Particle Physics.* Cambridge University Press, 2013 (cited on page 7).

[22] *Particle Data Group listing.* URL: `https://pdg.lbl.gov/2022/tables/contents_tables.html` (visited on 02/09/2023) (cited on page 8).

[23] G Konrad et.al. The PERC collaboration. "Neutron Decay with PERC: a Progress Report". In: (2012). DOI: `10.1088/1742-6596/340/1/012048` (cited on page 8).

[24] S. Kotochigova W.C. Martin A. Musgrove and J.E. Sansonetti. "Electronic structure of the elements". In: (2022). URL: `https://pdg.lbl.gov/2021/web/viewer.html?file=../reviews/rpp2021-rev-elements-electronic-struct.pdf` (cited on pages 10, 13).

[25] R.G. Alsmiller Jr. T.W. Armstrong. "An approximate density-effect correction for the ionization loss of charged particles". In: (May 30, 1970). DOI: `10.1016/0029-554X(70)90365-4` (cited on pages 10, 29).

[26] Erik Brücken and Timo Hildén. "GEM Foil Quality Assurance For The ALICE TPC Upgrade". In: (2017). DOI: `10.1051/epjconf/201817403004` (cited on page 13).

[27] *12.6 Bonding in Metals and Semiconductors - describing the electrical properties of a solid using band theory.* URL: https://saylordotorg.github.io/text_general-chemistry-principles-patterns-and-applications-v1.0/s16-06-bonding-in-metals-and-semicond.html (visited on 01/24/2023) (cited on pages 14, 17).

[28] *Why Do We Use Semiconductors Instead of Conductors in Electronic Circuit Design.* URL: https://www.elprocus.com/why-do-we-use-semiconductors-instead-of-conductors-in-electronic-circuit-design/ (visited on 01/15/2023) (cited on page 15).

[29] R.F. Pierret. *Semiconductor Device Fundamentals.* Addison-Wesley, 1996, pp. 214, 204. ISBN: 9780201543933. URL: https://books.google.de/books?id=dh3CQgAACAAJ (cited on pages 15, 16, 19, 20, 29).

[30] Robert Wittmann. *Miniaturization Problems in CMOS Technology: Investigation of Doping Profiles and Reliability.* Technical University Vienna, 2007. URL: https://www.iue.tuwien.ac.at/phd/wittmann/diss.html (cited on pages 15–17).

[31] Kwok K. Ng S.M. Sze. *Physics of Semiconductor Devices.* John Wiley & Sons, Inc., 2006. DOI: https://onlinelibrary.wiley.com/doi/book/10.1002/0470068329 (cited on page 16).

[32] *Properties of silicon and silicon wafers.* URL: https://www.el-cat.com/silicon-properties.htm (visited on 02/05/2023) (cited on pages 16, 20, 31).

[33] Hermann Kolanoski and Norbert Wermes. *Particle Detectors, Fundamentals and Applications.* Oxford University Press, 2020. URL: https://global.oup.com/academic/product/particle-detectors-9780198858362 (cited on page 16).

[34] *Doping (semiconductor).* URL: https://en.wikipedia.org/wiki/Doping_(semiconductor) (visited on 01/27/2023) (cited on page 17).

[35] R. Nave. *HyperPhysics, P-N Junction.* 2017. URL: http://hyperphysics.phy-astr.gsu.edu/hbase/Solids/pnjun.html (visited on 02/16/2023) (cited on page 18).

[36] *Built-In Potential: Aprupt pn junction.* URL: https://alhaytlna.blogspot.com/2017/03/pn-junction-abrupt.html (visited on 02/16/2023) (cited on page 18).

[37] *The NIST Reference on Constants, Units, and Uncertainty.* URL: https://physics.nist.gov/cgi-bin/cuu/Value?ep0 (visited on 01/20/2023) (cited on pages 19, 20).

[38] *Characteristics Of PN Junction.* URL: https://www.daenotes.com/electronics/basic-electronics/formation-depletion-layer-diode (visited on 02/19/2023) (cited on page 20).

[39] ALICE ITS ALPIDE development team. "ALPIDE Operations Manual". In: (2016) (cited on pages 21–23, 31, 34, 36, 44).

[40] Miljenko Suljic. "Study of Monolithic Active Pixel Sensors for the Upgrade of the ALICE Inner Tracking System". In: (Nov. 15, 2017). URL: http://cds.cern.ch/record/2303618/ (cited on pages 25, 26, 48, 51, 53).

[41] *A case of Improved Beam Control at COSY Jülich*. URL: https://www.cosylab.com/2021/06/21/a-case-of-improved-beam-control-at-cosy-julich/ (visited on 02/09/2023) (cited on page 27).

[42] *Deuteron mass energy equivalent in MeV*. URL: https://physics.nist.gov/cgi-bin/cuu/Value?mdc2mev (visited on 02/21/2023) (cited on page 27).

[43] Lukasz Maczewski. "Measurements and simulations of MAPS (Monolithic Active Pixel Sensors) response to charged particles - a study towards a vertex detector at the ILC". In: (May 20, 2010). DOI: 10.48550/arXiv.1005.3710 (cited on pages 29, 32, 60).

[44] Even Hunnes Helgesen Hansen. "Charge Diffusion Modelling for a Monolithic Active Pixel Sensor Detector with Application to Proton CT". In: (Feb. 2017). URL: https://ntnuopen.ntnu.no/ntnu-xmlui/bitstream/handle/11250/2434108/16246_FULLTEXT.pdf (cited on pages 29, 32, 33).

[45] IOP Publishing. *ALICE tracks new territory*. July 7, 2021. URL: https://cerncourier.com/a/alice-tracks-new-territory/ (cited on pages 29, 59).

[46] R. L. Workman et al. "Review of Particle Physics". In: *PTEP* 2022 (2022), p. 083C01. DOI: 10.1093/ptep/ptac097 (cited on page 29).

[47] Particle Data Group. *Atomic and nuclear properties of silicon (Si)*. 2022. URL: https://pdg.lbl.gov/2022/AtomicNuclearProperties/HTML/silicon_Si.html (cited on pages 29, 42).

[48] *Electrical properties of Silicon*. URL: http://www.ioffe.ru/SVA/NSM/Semicond/Si/electric.html (visited on 02/22/2023) (cited on pages 30, 36).

[49] D. Dannheim et al. "Combining TCAD and Monte Carlo methods to simulate CMOS pixel sensors with a small collection electrode using the Allpix2 framework". In: *Nuclear Instruments and Methods in Physics Research Section A: Accelerators, Spectrometers, Detectors and Associated Equipment* 964 (2020). ISSN: 0168-9002. DOI: 10.1016/j.nima.2020.163784. URL: https://www.sciencedirect.com/science/article/pii/S0168900220303181 (cited on page 36).

[50] B. Blidaru. personal communication. Jan. 30, 2023 (cited on page 36).

[51] Y. Liu et.al. "EUDAQ2 - A flexible data acquisition software framework for common test beams". In: *Journal of Instrumentation* 14.10 (Oct. 2019). DOI: 10.1088/1748-0221/14/10/P10033 (cited on page 40).

[52] D. Dannheim et al. "Corryvreckan: a modular 4D track reconstruction and analysis software for test beam data". In: *J. Instr.* P03008 (16 2021). DOI: `10.1088/1748-0221/16/03/P03008` (cited on page 40).

[53] Maurice Donner. "Tracking Cosmic Muons with the ALICE Pixel Detector A Study of Monolithic Active Pixel Sensors and Telescope Alignment". Mar. 2021. URL: `https://www.physi.uni-heidelberg.de/Publications/M_Donner_BachelorThesis.pdf` (cited on page 42).

[54] Particle Data Group. *Atomic and nuclear properties of air (dry, 1 atm).* 2022. URL: `https://pdg.lbl.gov/2022/AtomicNuclearProperties/HTML/air_dry_1_atm.html` (cited on page 42).

[55] L.P. Ekström S.Y.F. Chu and R.B. Firestone. *The Lund/LBNL Nuclear Data Search.* Feb. 1999. URL: `http://nucleardata.nuclear.lu.se/toi/index.asp` (cited on pages 43, 62).

[56] M. J. Berger et al. "Main Alpha Particle Tables". In: *Reports of the International Commission on Radiation Units and Measurements* os-25.2 (1993), pp. 183–257. DOI: `10.1093/jicru\_os25.2.183`. URL: `https://physics.nist.gov/PhysRefData/Star/Text/ASTAR.html` (cited on pages 43, 52–54).

[57] R. Diener et al. "The DESY II test beam facility". In: *Nuclear Instruments and Methods in Physics Research Section A: Accelerators, Spectrometers, Detectors and Associated Equipment* 922 (2019). ISSN: 0168-9002. DOI: `10.1016/j.nima.2018.11.133`. URL: `https://www.sciencedirect.com/science/article/pii/S0168900218317868` (cited on page 44).

[58] Hamamatsu Photonics K.K. *What is photon shot noise?* Dec. 2022. URL: `https://camera.hamamatsu.com/eu/en/learn/technical_information/thechnical_guide/photon_shot_noise.html` (cited on page 49).

[59] Eckert & Ziegler Nuclitec GmbH. *Verkaufszeichnung Demonstrationsstrahler VZ-2297-001.* Feb. 15, 2023 (cited on page 52).

[60] P.K.F. Grieder. *Cosmic rays at earth: researchers reference manual and data book.* ELSEVIER SCINECE B.V., 2001. URL: `http://theor.jinr.ru/~vnaumov/Eng/JINR_Lectures/books/Grieder2001.pdf` (cited on page 61).

[61] G. Weber. *X-Ray attenuation & absorption calculator.* URL: `http://web-docs.gsi.de/~stoe_exp/web_programs/x_ray_absorption/index.php` (visited on 02/03/2023) (cited on page 62).

Acknowledgment

Firstly, I would like to thank Prof. Dr. Silvia Masciocci, who gave me the opportunity to work in the hardware section of the ALICE at GSI group for my bachelor thesis. I am grateful for the motivating and understanding attitude presented to me for the entirety of my bachelor work and the project internship. In particular, I am thankful for the opportunity to visit the ALICE cavern at CERN, and to participate in the COSY testbeam, which was an absolutely thrilling experience for me personally. Also, I would like to thank Kai Schweda for accepting to be second corrector of this thesis.

Secondly, I would like to thank Mihail Bogdan Blidaru and Pascal Becht for relentlessly taking time out of their schedules for error-checking of my work and helping me correct this thesis. This help was of high quality and is greatly appreciated.

I also thank every colleague working with me in the office during this time, for creating a very happy and accepting work atmosphere.
I learned a lot from their combined knowledge of the hardware used, especially in the context of testbeams and the Linux operating system. In this aspect, I would like to explicitly name Maurice Donner for introducing me to helpful material in this regard. Thanks to him, Leonie Scheidweiler and others, I have learned to utilize the modern computer to an extent i never previously thought possible.

During all this time, my family always actively supported me. Without help from my loving parents I would not be in Heidelberg studying Physics, a topic very important and interesting to me. My family will always occupy a place in my thoughts, working towards prosperous times, hoping the stone will stay unbroken.

健全なる「魂」は、
健全なる精神と
健全なる肉体に宿る
ソウルイーター・マカ・アルバーン